Approximate Projection Methods: Part I. Inviscid Analysis *

Ann S. Almgren, John B. Bell, and William Y. Crutchfield †

Lawrence Berkeley National Laboratory, Berkeley, California

Abstract

The use of approximate projection methods for modeling low Mach number flows avoids many of the numerical complications associated with exact projection methods, but introduces additional design choices in developing a robust algorithm. In this paper we first explore these design choices in the setting of inviscid incompressible flow using several computational examples. We then develop a framework for analyzing the behavior of the different design variations and use that analysis to explain the features observed in the computations. As part of this work we introduce a new variation of the approximate projection algorithm that combines the advantages of several of the previous versions.

1 Introduction

The term "projection methods" refers to a class of fractional step algorithms for modeling unsteady low Mach number flows characterized by a divergence constraint on the velocity field. In these methods an intermediate velocity field is constructed by advancing the momentum equations in time without enforcing the constraint. In the next step of the algorithm this field is projected back onto the constraint.

Projection methods have been used for incompressible flow modeling for several decades, but approximate projection methods have appeared only in the past few years. They have been numerically tested on a number of flows in two and three spatial dimensions, but adequate analysis of their properties has been lacking to date. In this paper we provide an analytical basis for understanding the behavior of approximate projection methods, and some of the design decisions that accompany their use.

For the purposes of this paper we will focus on inviscid, constant density flows, with numerical examples in two dimensions. In the second paper in this series we will extend the analysis to the modeling of viscous flows. The extension to variable density flows, and adaptive projection methods with subcycling in time, will follow.

*This work was supported by the Applied Mathematical Sciences Program of the DOE Office of Mathematics, Information, and Computational Sciences, under contract DE-AC03-76SF00098.

†Contact information: MS 50A-1148, LBNL, 1 Cyclotron Rd., Berkeley, CA 94720. ASAlmgren@lbl.gov, JBBell@lbl.gov, WYCrutchfield@lbl.gov.

In the original projection method developed by Chorin [5] and Temam [23] the projection step of the algorithm is specified by defining discrete operators $\mathbf{D}$ and $\mathbf{G}$, approximating divergence and gradient, respectively, which are skew-adjoint; i.e., $\mathbf{D} = -\mathbf{G}^T$. With this definition the discrete projection, $\mathbf{P} = \mathbf{I} - \mathbf{G}(\mathbf{DG})^{-1}\mathbf{D}$ (with boundary conditions implicitly defined by the the flow problem), is a discrete orthogonal projection on the finite-dimensional space of vector fields defined on the mesh. In Chorin's formulation both pressure and velocity are specified at nodes and central differences are used for the definition of $\mathbf{D}$ and $\mathbf{G}$. This results in an expanded five-point stencil for the discrete Laplacian, $L = \mathbf{DG}$, which must be inverted to apply the projection. This expanded stencil produces a local decoupling of the mesh points and leads to a 2^d-dimensional kernel for $\mathbf{G}$ where d is the dimension of the problem. Bell, Colella, and Glaz [3] use a discretization of the projection based on a finite element method due to Fortin [7] which uses pressure defined on cell centers with velocities given at nodes. This approach produces a more compact stencil but also generates a local decoupling of the grid and *dim ker* $\mathbf{G} > 1$. (For two dimensional problems *dim ker* $\mathbf{G} = 2$.) Bell, Colella and Howell [4] use a fully cell-centered analog of Chorin's algorithm. This scheme exhibits a local decoupling; however, in the presence of Dirichlet boundary conditions, the cell-centered approximation eliminates the nonconstant elements in *ker* $\mathbf{G}$. (For periodic problems *dim ker* $\mathbf{G} = 2^d$ as in the original Chorin algorithm.)

In the absence of boundaries the additional elements in *ker* $\mathbf{G}$ are not a problem for incompressible flow modeling because the operator $(\mathbf{DG})^{-1}$ is applied to a vector field that lies in the range of $\mathbf{D}$. In the presence of boundaries, however, the nonconstant elements in the kernel introduce additional, artificial compatibility constraints on the boundary of the physical domain. In addition, for more complex low Mach number models, such as low Mach number combustion, a term that is not in the range of the divergence operator is often added to the divergence constraint to represent the expansion or contraction of the fluid due to additional physics. The presence of this additional source term can result in marked oscillations in the solution, as noted by Lai [10] and Lai, Bell and Colella [11]. An additional difficulty associated with the local decoupling is that the nonstandard discretizations of $\mathbf{DG}$ require specialized iterative procedures that properly respect the stencil that is used. (See [4, 8] for a discussion of such a procedure.)

Almgren *et al.* [2] first introduced the notion of an approximate projection to circumvent the numerical difficulties with exact discrete projections. Approximate projections are defined by replacing the projection operator $\mathbf{P}$ by an approximation $\tilde{\mathbf{P}} = \mathbf{I} - \mathbf{G}(L)^{-1}\mathbf{D}$, where L is an approximation to but not identically $\mathbf{DG}$. The approximate projection methods discussed here were designed to operate on cell-centered co-located velocities, to avoid any local decoupling of the stencils, to provide a symmetric discretization of the potential flow inherent in inhomogeneous boundary conditions, and to generate a linear system that fits the framework of conventional fast iterative techniques (e.g. multigrid) for second-order elliptic equations.

The approximate projection introduced by Almgren *et al.* [2] defines pressure on nodes and uses a finite element formulation with bilinear basis functions to derive a nine-point (in two dimensions) stencil for the Laplacian operator. The finite element derivation gives a characterization of this projection as an exact discrete projection onto an enriched space followed by an L^2 projection onto a subspace corresponding to piecewise constant velocity fields. This derivation provides an analytic characterization of the effect of the "approximateness" and proves stability of the approximation. A standard five-point nodal approximation to the Laplacian can also be used. This approximation can be constructed in a similar manner by specifying pressure to be piecewise linear on the standard triangularization of a square mesh. The analogous three-dimensional seven-point nodal discretization has been successfully used by Almgren *et al.* in [1], but lacks the finite element derivation.

Lai [10] introduced a cell-centered approximate projection where pressure is defined at cell centers and which uses a standard five-point centered-difference stencil for the Laplacian. The stability of such a scheme was shown in [10]; this approximate projection has been used by Martin [12] in an adaptive projection algorithm, and a variation of this (with the same L but a higher-order $\mathbf{D}$) by Minion [14] in an adaptive scheme.

Approximate projections have also been successfully applied to more general low Mach number flows arising in combustion (e.g.,[17, 18]) and atmospheric flow (e.g.,[21, 22]). However, in spite of these successful applications, approximate projection algorithms are not without their own problems. Adopting an approximate projection approach introduces a number of design choices that are not relevant for an exact discrete projection. When applied to "difficult" problems or to long-time integrations, approximate projection algorithms can produce poor quality results. Rider discusses some of these design choices for the five-point cell-centered scheme [19] and describes a collection of filtering techniques to deal with artifacts he observes in numerical tests [20].

The goal of this paper is to develop an analytical framework to explain the performance of different variations of approximate projection methods and to explore methods for improving their behavior. In the next section we will give a brief overview of projection methods using an exact projection; in Section 3 we introduce several different formulations of approximate projection schemes. In the following two sections we present a temporal analysis of approximate projections, then a spatial analysis of the three specific approximate projections discussed here. In Section 6 we discuss issues related to the coupling between the advection scheme and the choice of approximate projection, and in Section 7 we present our conclusions and discussion.

2 Overview of Exact Projection Methods

In this paper we will consider constant density, inviscid, incompressible flow, governed by

$$\mathbf{U}_t + (\mathbf{U} \cdot \nabla)\mathbf{U} + \nabla p = 0, \tag{2.1}$$

$$\nabla \cdot \mathbf{U} = 0, \tag{2.2}$$

where (in two dimensions) $\mathbf{U} = (u, v)$ and p represent the velocity and pressure, respectively.

The projection method is a fractional step scheme for solving (2.1)-(2.2). In the advection step we solve (2.1) without enforcing the constraint. In the projection step, we then apply a projection to the intermediate velocity field to enforce the constraint. For the advection step we solve

$$\frac{\mathbf{U}^{*,n+1} - \mathbf{U}^n}{\Delta t} + [(\mathbf{U} \cdot \nabla)\mathbf{U}]^{n+1/2} = -\mathbf{G}p^{n-1/2} \tag{2.3}$$

for the intermediate velocity $\mathbf{U}^{*,n+1}$. The pressure gradient is evaluated at $t^{n-1/2}$ and is treated as a source term. For the computations presented here, the advection term, $\mathbf{N}^{n+1/2} = [(\mathbf{U}\cdot\nabla)\mathbf{U}]^{n+1/2}$, is approximated at time $t^{n+1/2}$ to second-order in space and time using an explicit predictor-corrector scheme described in Appendix A. (We note that the analysis presented later in the paper is applicable when other approaches are used to compute $\mathbf{N}^{n+1/2}$. Experiments with different options in the predictor-corrector scheme presented in section 6 are suggestive of the degree to which the conclusions reached here are applicable to other methods.)

The velocity field $\mathbf{U}^{*,n+1}$ is not, in general, divergence-free. In the projection step of the algorithm the intermediate velocity field can be decomposed into a discrete gradient of a scalar potential and a discretely divergence-free vector field which correspond, respectively, to the new pressure gradient and the new velocity, i.e.,

$$\begin{aligned}\mathbf{U}^{n+1} &= \mathbf{P}\mathbf{U}^{*,n+1},\\ \Delta t\,\mathbf{G}p^{n+1/2} &= \Delta t\,\mathbf{G}p^{n-1/2} + (\mathbf{I}-\mathbf{P})\mathbf{U}^{*,n+1}\end{aligned}$$

To apply the projection operator we solve $\mathbf{D}\mathbf{G}\phi = \mathbf{D}\mathbf{V}$ for a scalar field ϕ, where, in this case, $\mathbf{V} = \mathbf{U}^{*,n+1}$. We then define the divergence-free part of $\mathbf{V}$, in this case $\mathbf{U}^{n+1}$, by $\mathbf{V}_d = \mathbf{V} - \mathbf{G}\phi$. By construction $\mathbf{D}\mathbf{V}_d = 0$; thus, $\mathbf{U}^{n+1}$ exactly satisfies the discrete form of divergence constraint.

3 Approximate Projections

For an exact projection, $\mathbf{V}$ can take many forms, all of which lead to exactly the same solution (assuming an exact solution of the resulting Poisson equation). Two natural candidates for $\mathbf{V}$ are the velocity itself or the update to velocity. One could also modify each of these by removing the pressure gradient component of the update. Specifically, one might choose any of the following (with the Δt scaling for convenience):

$$\begin{aligned}(1)\quad \mathbf{V} &= \frac{\mathbf{U}^{*,n+1}}{\Delta t}\\ (2)\quad \mathbf{V} &= \frac{\mathbf{U}^{*,n+1}}{\Delta t} + \mathbf{G}p^{n-1/2}\\ (3)\quad \mathbf{V} &= \frac{\mathbf{U}^{*,n+1} - \mathbf{U}^n}{\Delta t}\\ (4)\quad \mathbf{V} &= \frac{\mathbf{U}^{*,n+1} - \mathbf{U}^n}{\Delta t} + \mathbf{G}p^{n-1/2},\end{aligned}$$

Then, after solving $\mathbf{D}\mathbf{G}\phi = \mathbf{D}\mathbf{V}$ and setting $\mathbf{V}_d = \mathbf{V} - \mathbf{G}\phi$, the new velocity and pressure would be defined, respectively, by

$$\begin{aligned}(1)\quad \mathbf{U}^{n+1} &= \Delta t\,\mathbf{V}_d, & p^{n+1/2} &= p^{n-1/2} + \phi\\ (2)\quad \mathbf{U}^{n+1} &= \Delta t\,\mathbf{V}_d, & p^{n+1/2} &= \phi\\ (3)\quad \mathbf{U}^{n+1} &= \mathbf{U}^n + \Delta t\,\mathbf{V}_d, & p^{n+1/2} &= p^{n-1/2} + \phi\\ (4)\quad \mathbf{U}^{n+1} &= \mathbf{U}^n + \Delta t\,\mathbf{V}_d, & p^{n+1/2} &= \phi\end{aligned}$$

For approximate projections the choice of $\mathbf{V}$ has a nontrivial effect on the solution. Because the approximate projection operators are second-order accurate approximations to an exact projection, the methods which result from each choice of $\mathbf{V}$ are all second-order accurate for smooth problems, but not identical.

For the sake of clarity, we here introduce some notation for the different spatial and temporal discretizations. We will refer to the approximate projection with the nine-point nodal discretization of L as **N9**, that with the five-point nodal discretization of L as **N5**, and that with the five-point cell-centered discretization of L as **C5**. In addition, for all results we will specify which version of $\mathbf{V}$ is being projected; e.g., **N9_3** will indicate the nine-point nodal scheme, version (3) of $\mathbf{V}$. In the published literature, Almgren *et al.* [1, 2] have presented results using **N5_3** and **N9_3**; Martin [12] used **C5_2**, and Minion [14] has used **C5_4**. Rider [19] presents extensive testing of **C5_1-4** in conjunction with the development of filters to reduce numerical artifacts.

We also note here that for each of the approximate projection operators, $\widetilde{\mathbf{P}}$, there is a corresponding exact discrete projection $\mathbf{P} = I - \mathbf{G}(\mathbf{DG})^{-1}\mathbf{D}$ defined using the same $\mathbf{D}$ and $\mathbf{G}$ used to define $\widetilde{\mathbf{P}}$. We will refer to the exact nodal projection as **N_EX** and the exact cell-centered projection as **C_EX.**

To demonstrate the second-order accuracy of the different versions of the approximate projections, we present results from a time-periodic test case with diagonally translating vortices. The initial data is

$$\begin{aligned} u(x,y) &= 1 - 2\cos(x)\sin(y) \\ v(x,y) &= 1 + 2\sin(x)\cos(y) \end{aligned}$$

on a square domain, 2π x 2π. The exact solution to the Euler equations with this initial data is

$$\begin{aligned} u_{ex}(x,y,t) &= 1 - 2\cos(x-t)\sin(y-t), \\ v_{ex}(x,y,t) &= 1 + 2\sin(x-t)\cos(y-t), \\ p_{ex}(x,y,t) &= -\cos(2(x-t)) - \sin(2(y-t)). \end{aligned}$$

For each version of $\mathbf{V}$ and each approximate projection we present results at three different resolutions: 32^2, 64^2, and 128^2. In all cases we use fourth-order unlimited slopes in the predictor. The L^2 norms of the error in u and p_x are shown in Figures 1 and 2, respectively. It is clear that each method is second-order accurate; in addition, it is evident that there are differences between the solutions resulting from the different forms of the projections, most noticeably **C5_4**. We will explain these differences in the next two sections.

As demonstrated above, the difficulty with using approximate projections is not a question of formal accuracy on smooth problems. Instead, problems tend to appear as a buildup of "noise" during longer time integrations of more complex problems. To illustrate this behavior we present results from each of the approximate projections run on on a more complex problem, namely the inviscid dynamics of a random initial distribution of vorticity. A key feature of this problem is that it contains substantially more high frequency content than the previous test case. The initial data

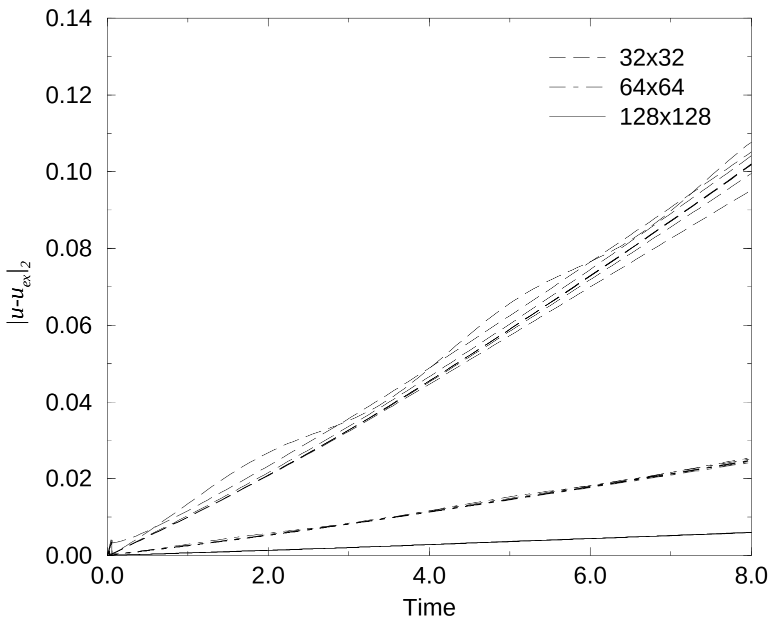

(a) $||u - u_{ex}||_2$ for cases **N5_1-4**, **N9_1-4** and **C5_1-3**.

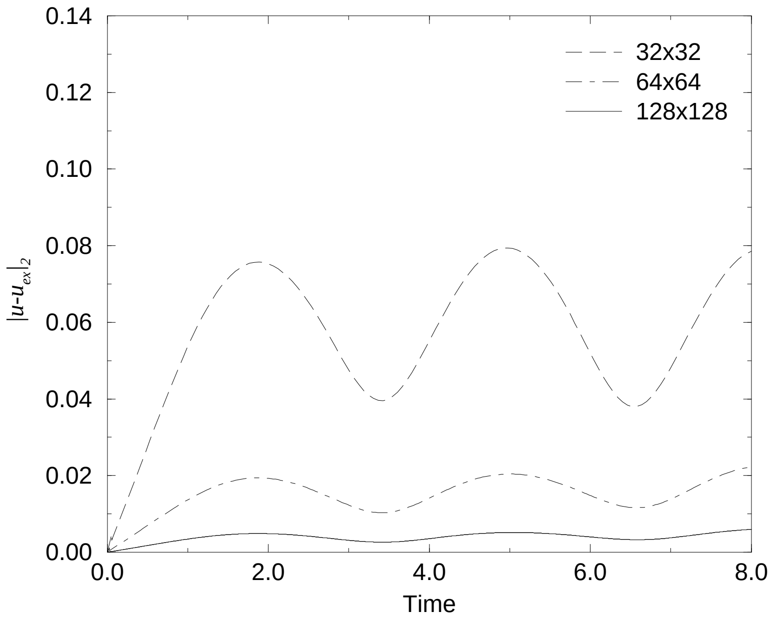

(b) $||u - u_{ex}||_2$ for case **C5_4**.

Figure 1: L^2 norm of error in u for the translating vortices problem.

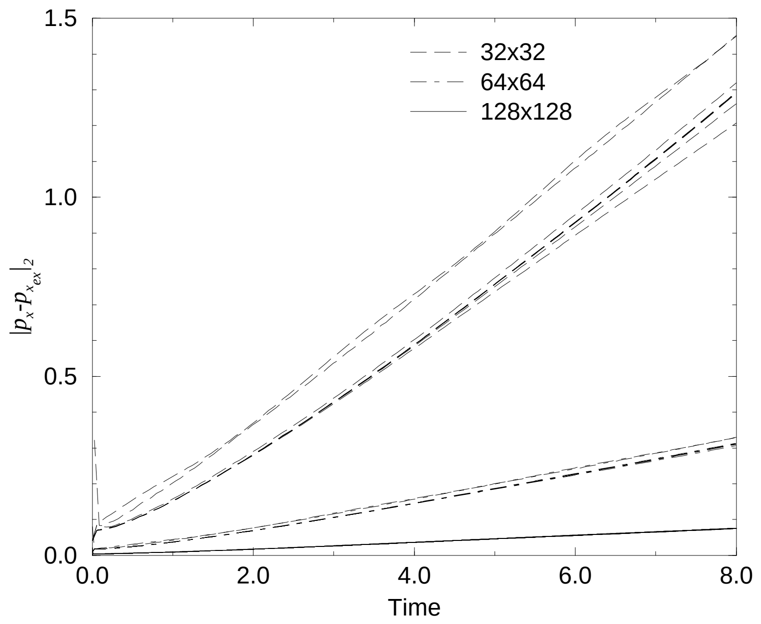

(a) $||p_x - p_{x\,ex}||_2$ for cases **N5_1-4**, **N9_1-4** and **C5_1-3**.

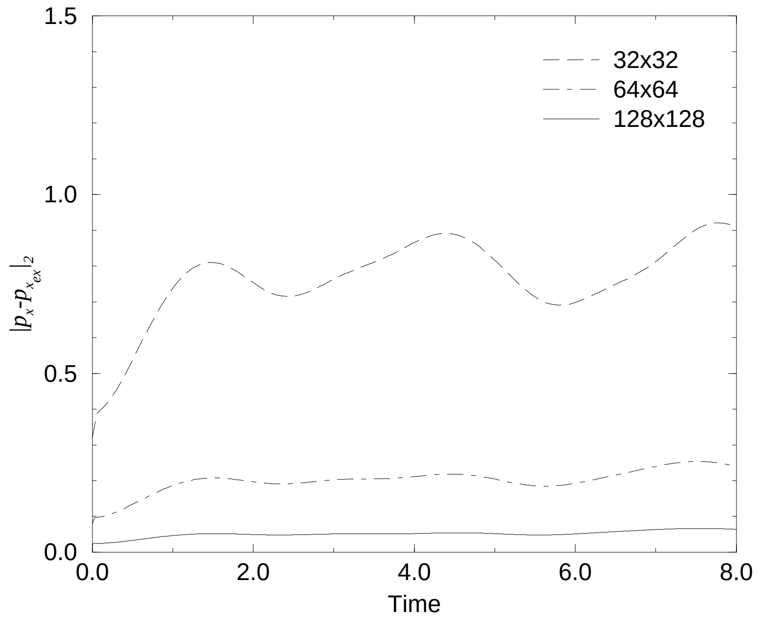

(b) $||p_x - p_{x\,ex}||_2$ for case **C5_4**.

Figure 2: L^2 norm of error in p_x for the translating vortices problem.

for this problem are given by specifying a random stream function with spectral characteristics defined by

$$\hat{\psi}(k) = \frac{\omega}{|k|(1 + (|k|/6)^4)}$$

where ω is a normally distributed random variable mapped into the complex domain with the appropriate symmetries so that the inverse Fourier transform of $\hat{\psi}$ is a real function, ψ. We then define $\mathbf{U}^0$ as the discrete curl of ψ. The initial data for this problem are similar to the initial data used to test the decay at high Reynolds number of the two-dimensional Navier-Stokes equations to the sinh-Poisson mean field equations derived by Joyce and Montgomery [9]. This type of problem has been studied extensively by a number of authors. (See the early work by McWilliams [13] and other studies such as Montgomery *et al.* [15] and the references cited therein.) We note that the key difference between the initial data we have constructed and the data used in the above studies is that in those studies the kinetic energy scales like k^{-3} for large k, but here we are imposing a more rapid decay for large k. This more rapid decay reduces the very high frequency components of the solution so that the computations are less sensitive to the behavior of the advection scheme. (Results similar to those presented here are also obtained with the richer spectrum but the anomalies occur at higher resolution and longer time integrations, which are prohibitive for extensive testing.)

We examine the evolution of the solution from time $t = 0$ to 10, over which time the initial random vorticity essentially coalesces into two smooth patches of counter-rotating vorticity. In Figure 3 we show raster plots of the vorticity and p_x at $t = 0$ and $t = 10$ on a 64^2 grid calculated with **N9_2.** The domain is the unit square with doubly periodic boundary conditions, and all calculations are run with CFL = 0.9.

Several variations of the approximate projection produce poor results for this problem. In particular, in Figures 4 through 6 we show the vorticity and p_x at $t = 10$ as calculated using **N9_1**, **C5_3**, and **N5_4**, respectively. In Figure 4, checkerboarding (high frequency error in the solution) is evident in the pressure gradient and to a lesser extent in the vorticity. Similarly, in Figure 5, high frequency error is visible, though due to the cell-centered discretization the error appears more as "striping" than checkerboarding in the vorticity. Figure 6 shows more coherently structured but equally unphysical features in both the vorticity and pressure gradient.

In Figure 7 we plot the numerical divergence of velocity (calculated in each case with the same $\mathbf{D}$ as the approximate projection used) as a function of time for all twelve cases (**C5_1-4, N9_1-4, N5_1-4**), at resolutions 64^2 and 128^2. While the divergence does decrease with increased resolution, the differences between the variations of the projection persist. (In fact **N5_1** becomes more unstable at higher resolution.) An examination of all twelve cases indicates that plots of the solutions with relatively small divergence are comparable to Figure 3; plots of solutions with relatively larger divergence are comparable to Figures 4 through 6. It is evident that the divergence is a useful indicator of solution quality for problems such as this one for which an exact solution is not known.

For the random initial vorticity problem, it appears that the only acceptable formulation of the approximate projection across all three discretizations is version (2). Version (2), however, is not without its drawbacks. As we will see analytically in the next section, the divergence of the

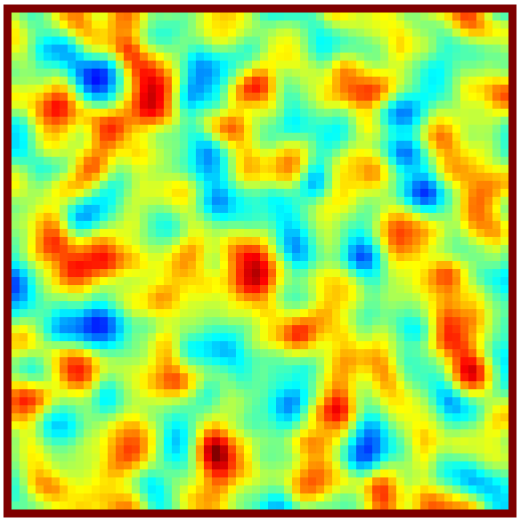

(a) Vorticity at $t = 0$.

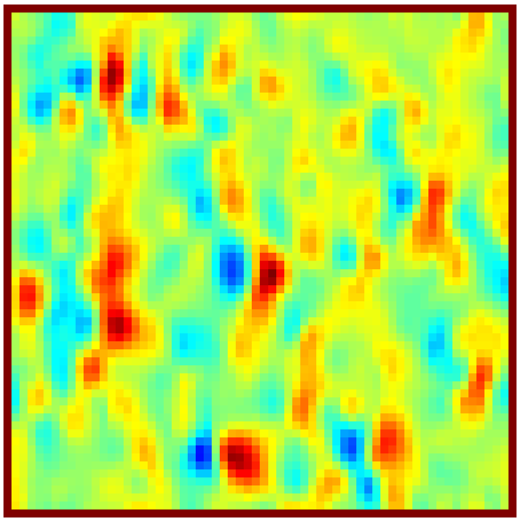

(b) p_x at $t = 0$.

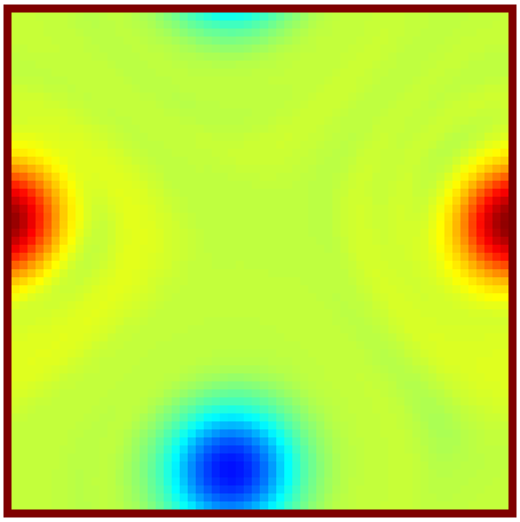

(c) Vorticity at $t = 10$.

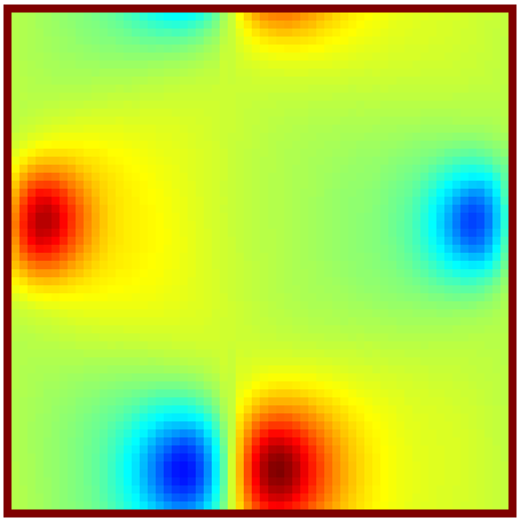

(d) p_x at $t = 10$.

Figure 3: Vorticity and p_x at $t = 0$ and $t = 10$ for the **N9_2** case of the random initial vorticity calculation at resolution 64^2.

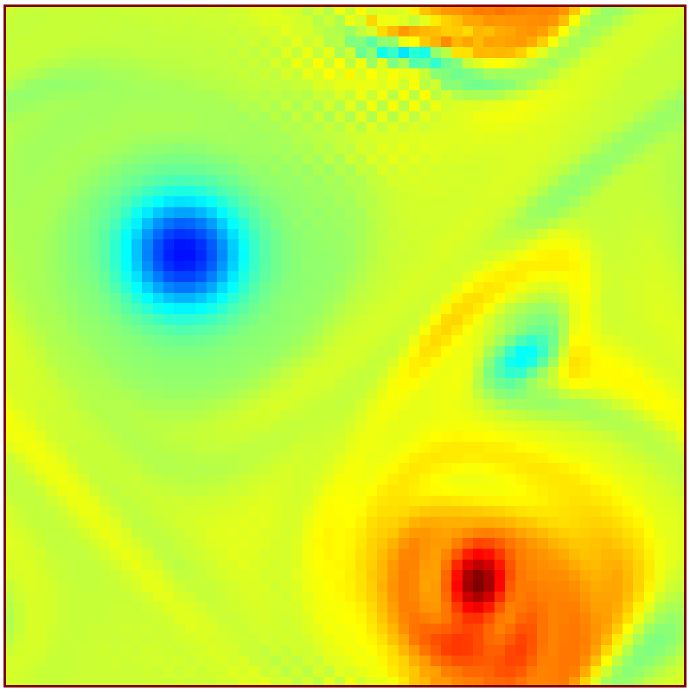

(a) Vorticity at $t = 10$.

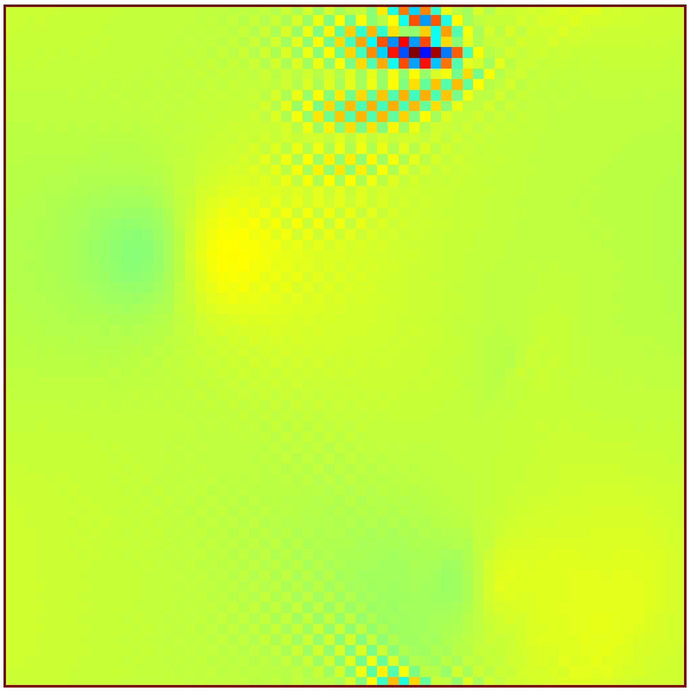

(b) p_x at $t = 10$.

Figure 4: Vorticity and p_x at $t = 10$ for the **N9_1** case of the random initial vorticity calculation at resolution 64^2.

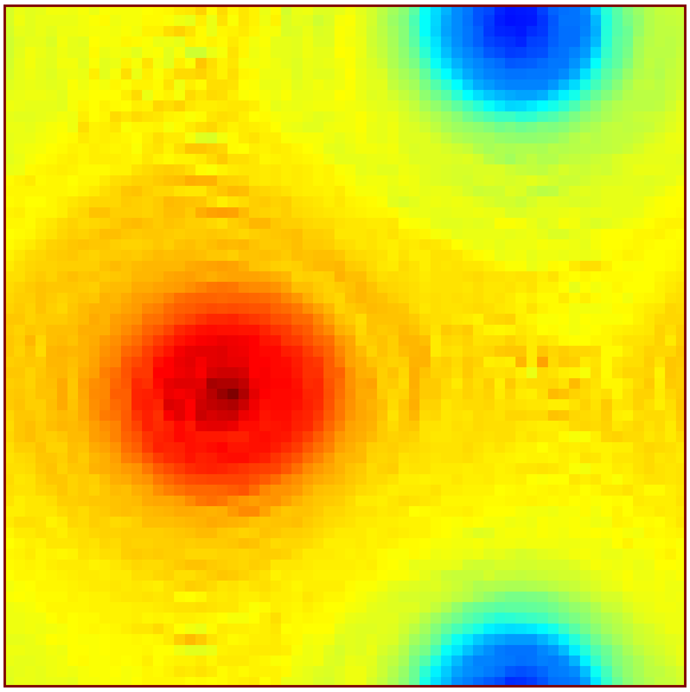

(a) Vorticity at $t = 10$.

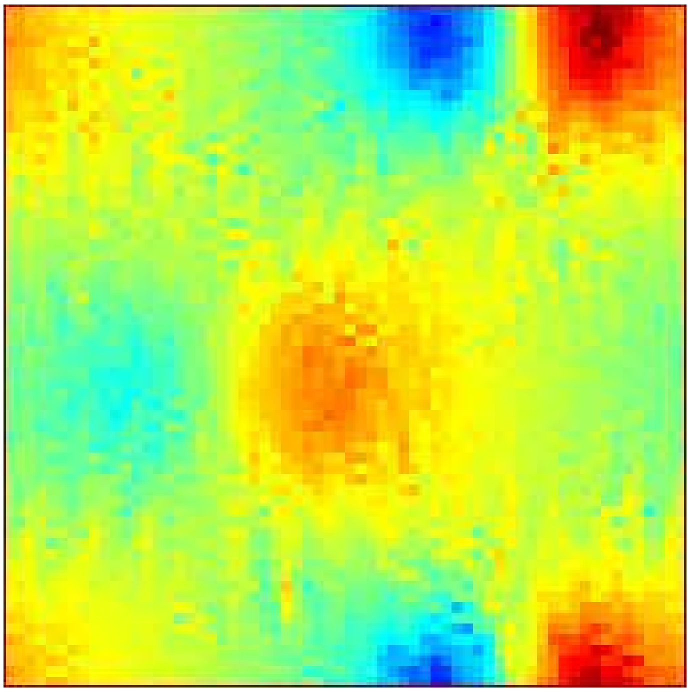

(b) p_x at $t = 10$.

Figure 5: Vorticity and p_x at $t = 10$ for the **C5_3** case of the random initial vorticity calculation at resolution 64^2.

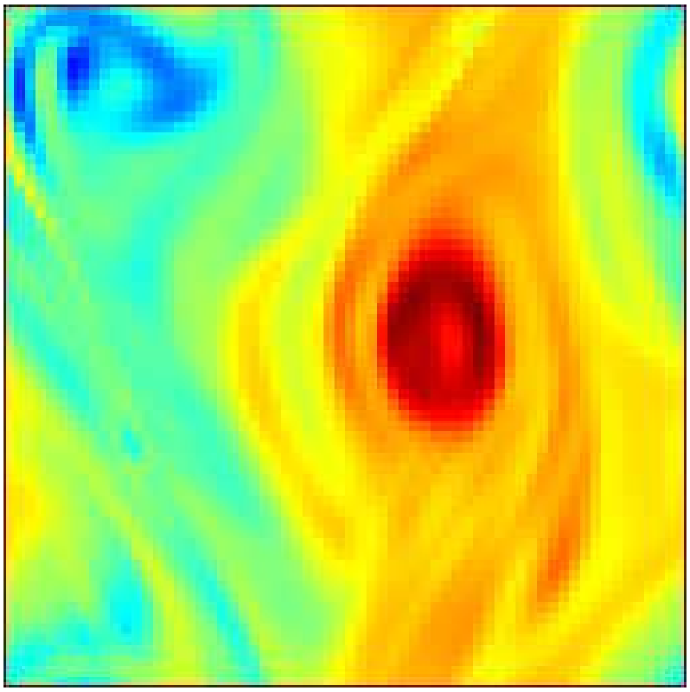

(a) Vorticity at $t = 10$.

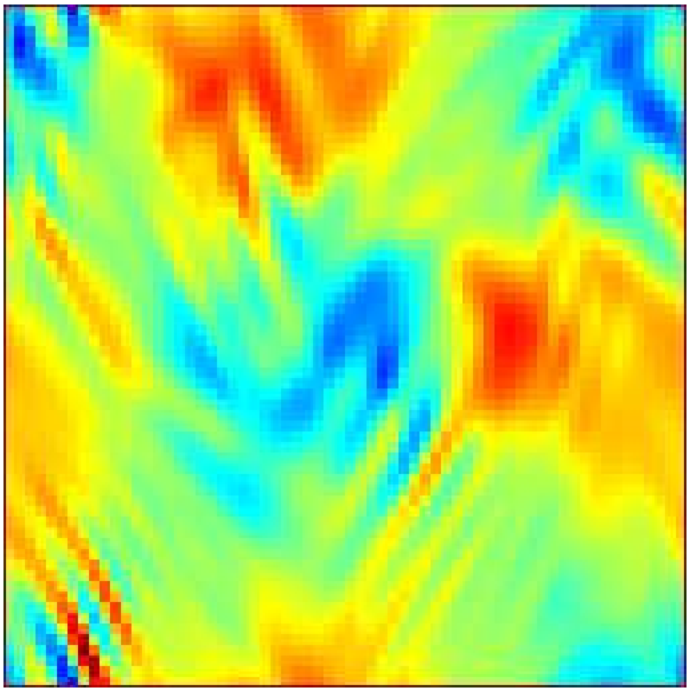

(b) p_x at $t = 10$.

Figure 6: Vorticity and p_x at $t = 10$ for the **N5_4** case of the random initial vorticity calculation at resolution 64^2.

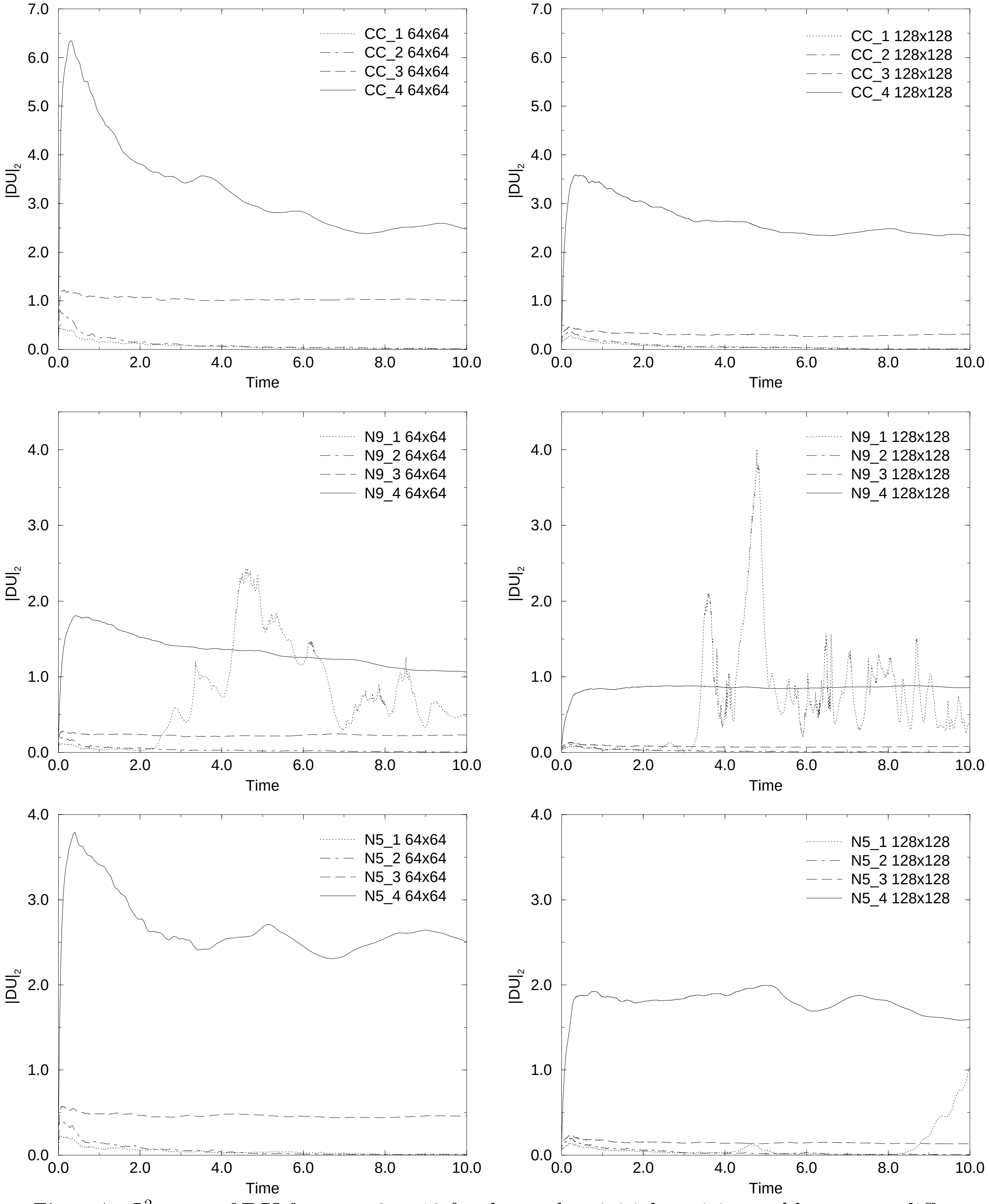

Figure 7: L^2 norm of $\mathbf{DU}$ from $t = 0$ to 10 for the random initial vorticity problem at two different resolutions.

solution found with version (2) is typically larger than when version (1) is used, provided version (1) remains stable. To demonstrate this, we consider a very simple steady problem for which we know the exact solution. The initial data (and steady solution) are

$$u_{ex} = \sin(y), \qquad v_{ex} = \cos(x).$$

To eliminate issues of predictor-projection coupling which will be discussed in Section 7, we here use the exact analytic solution to define the advective terms at each time step, i.e. we set $\mathbf{N}_{i,j}^{n+1/2} = (\cos(x_i)\cos(y_j), -\sin(x_i)sin(y_j))$ where $x_i = ih, y_j = jh$ with h the mesh spacing. All calculations are run with CFL $= 0.9$ and resolution 32^2.

Figure 8 shows the L^2 error in u from time $t = 0$ to 150 for versions (1) and (2) with each approximate projection. The solid curves using version (1) are indistinguishable in this figure from the x-axis; the three remaining curves were computed with version (2). Clearly the error grows steadily for version (2), while remaining essentially zero for version (1).

While the difference between versions (1) and (2) is especially noticeable for a steady problem, analogous behavior is seen in the initial iteration of the algorithm which is used to define the initial pressure field. At the beginning of a calculation, the initial velocity field is projected once to enforce the divergence constraint. Then an iteration is performed to compute $\mathbf{G}p^{-1/2}$. In each step of this iteration a full time step is taken; after the projection step the pressure field is updated, but the velocity is reset to its previous value.

If version (1) or (3) of the approximate projection is used, then in the limit as the number of iterations becomes infinite, the initial pressure converges to the correct value (that which would be found with infinitely many iterations of an exact projection). With versions (2) or (4), however, because these versions are nonincremental in pressure, the pressure does not converge, regardless of the number of iterations.

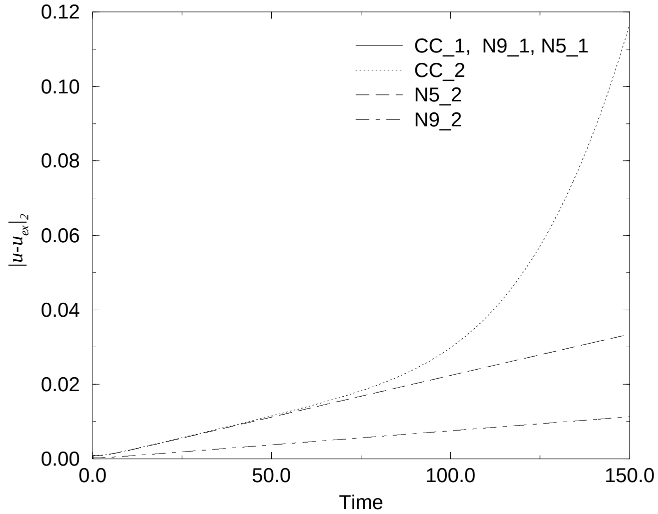

Figure 8: L^2 norm of the error in u from $t = 0$ to $t = 150$ from calculations of the steady problem. Curves using projection version (1) overlay the x-axis.

4 Temporal Analysis of Approximate Projections

The goal of this and the next section is to develop an analytical framework to explain the results of the computations presented in the previous section. The expressions presented by Rider [19] for the divergence of velocity suggest that version (1) should produce the lowest divergence, that versions (2) and (3) should produce similar results, and that version (4) should generate the highest divergence. These predictions hold true in some cases but do not fully explain the computations presented in the previous section or the computations in [19], specifically the lack of robustness of version (1) and the differences in behavior between versions (2) and (3).

In order to understand the behavior of the different variations of approximate projections, for each version we express the velocity and pressure gradient after n time steps, $\mathbf{U}^n$ and $\mathbf{G}p^{n-1/2}$, in terms of the initial data, $\mathbf{U}^0$ and $\mathbf{G}p^{-1/2}$, the advective updates at each time step, $\mathbf{N}^{i+1/2}$, and the approximate projection operator, $\widetilde{\mathbf{P}}$. These expressions are derived by substituting the expression for $\mathbf{U}^{*,n+1}$ from (2.3) into the definitions of $\mathbf{U}^{n+1}$ for each version of the approximate projection defined in Section 3. Successive substitution provides the desired characterization of each version of the algorithm. The results for each version are summarized in Tables 1 and 2.

The coefficients in the formula for $\mathbf{U}^n$ using version (1) are defined by the recursion relations

$$\mathbf{Q}_\alpha^n = \widetilde{\mathbf{P}}(\mathbf{Q}_\alpha^{n-1}) - (\mathbf{I} - \widetilde{\mathbf{P}})(\mathbf{Q}_\beta^{n-1}), \quad \mathbf{Q}_\beta^n = \widetilde{\mathbf{P}}(\mathbf{Q}_\alpha^{n-1} + \mathbf{Q}_\beta^{n-1}),$$

with starting values $\mathbf{Q}_\alpha^1 = \mathbf{Q}_\beta^1 = \widetilde{\mathbf{P}}$, $\mathbf{Q}_\alpha^2 = 2\widetilde{\mathbf{P}}^2 - \widetilde{\mathbf{P}}$, $\mathbf{Q}_\beta^2 = 2\widetilde{\mathbf{P}}^2$, $\mathbf{Q}_\alpha^3 = 4\widetilde{\mathbf{P}}^3 - 3\widetilde{\mathbf{P}}^2$ and $\mathbf{Q}_\beta^3 = 4\widetilde{\mathbf{P}}^3 - \widetilde{\mathbf{P}}^2$. Note that $\mathbf{Q}_\alpha^n$ and $\mathbf{Q}_\beta^n$ are polynomials in $\widetilde{\mathbf{P}}$ and that the coefficient of $\widetilde{\mathbf{P}}^n$ in each is 2^{n-1}. Note also that the sum of the coefficients in $\mathbf{Q}_\alpha^n$ is one, and the sum of the coefficients in $\mathbf{Q}_\beta^n$ is n.

The coefficients in the formula for $\mathbf{G}p^{n-1/2}$ using version (1) are defined by the recursion relations

$$\mathbf{Q}_\gamma^n = \widetilde{\mathbf{P}}(\mathbf{Q}_\gamma^{n-1}) - (\mathbf{I} - \widetilde{\mathbf{P}})(\mathbf{Q}_\delta^{n-1}), \quad \mathbf{Q}_\delta^n = \widetilde{\mathbf{P}}(\mathbf{Q}_\gamma^{n-1} + \mathbf{Q}_\delta^{n-1}),$$

with starting values $\mathbf{Q}_\delta^1 = -\widetilde{\mathbf{P}}$ and $\mathbf{Q}_\gamma^1 = (\mathbf{I} - \widetilde{\mathbf{P}})$.

It is clear there is a tradeoff in choosing any one form of $\mathbf{V}$. In the numerical results of the previous section, version (1) gives the smallest divergence of velocity when it remains stable; however, it suffers from a lack of robustness. Version (4), by contrast, defines the pressure gradient using only the most recent advection terms, as does an exact discrete projection, but produces very poor computational results. Version (2) appears to be robust and reliable but the velocity field, as seen in the steady example, can accumulate the imprint of the pressure gradient from previous times.

To date, approximate projection methods have followed the lead of exact projection methods in using a single projection to define both the new velocity and pressure. Here, however, motivated by the problems with each form, we introduce the concept of separate projections for the velocity and pressure. We propose an approximate projection method in which a version (1) projection is used to define the new velocity field, and a version (4) projection is then used to define the new pressure gradient. We will call this version (5). If the second projection is solved to full precision, this doubles the computational work of the projection step. However, in our numerical

Version	$\mathbf{U}^n =$
Exact	$\mathbf{U}^0 - \sum \mathbf{P}(\Delta t\ \mathbf{N}^{n+1/2-i})$
(1)	$\mathbf{U}^n = \mathbf{Q}_\rho^n \mathbf{U}^0 - \mathbf{Q}_\beta^n(\Delta t\ \mathbf{G}p^{-1/2}) - \sum_{i=1}^n \mathbf{Q}_\alpha^i(\Delta t\ \mathbf{N}^{n+1/2-i})$
(2)	$\widetilde{\mathbf{P}}^n \mathbf{U}^0 - \sum \widetilde{\mathbf{P}}^i(\Delta t\ \mathbf{N}^{n+1/2-i})$
(3)	$\mathbf{U}^0 - \sum \widetilde{\mathbf{P}}^i(\Delta t\ \mathbf{N}^{n+1/2-i}) - \sum \widetilde{\mathbf{P}}^i(\Delta t\ \mathbf{G}p^{-1/2})$
(4)	$\mathbf{U}^0 - \sum \widetilde{\mathbf{P}}(\Delta t\ \mathbf{N}^{n+1/2-i})$

Table 1: $\mathbf{U}^n$ in terms of $\mathbf{U}^0$, $\mathbf{G}p^{-1/2}$, and $\mathbf{N}$. All sums are from $i = 1$ to n unless otherwise noted.

Version	$\Delta t\ \mathbf{G}p^{n-1/2} =$
Exact	$-(\mathbf{I} - \mathbf{P})(\Delta t\ \mathbf{N}^{n-1/2})$
(1)	$-\Delta t\ \sum \mathbf{Q}_\gamma^i \mathbf{N}^{n+1/2-i} - \Delta t\ \mathbf{Q}_\delta^n \mathbf{G}p^{-1/2}$
(2)	$-(\mathbf{I} - \widetilde{\mathbf{P}})(\Delta t\ \mathbf{N}^{n-1/2})$ $+ (\mathbf{I} - \widetilde{\mathbf{P}})\widetilde{\mathbf{P}}^{n-1}\mathbf{U}^0 - \sum_{i=2}^n (\widetilde{\mathbf{P}}^{i-1} - \widetilde{\mathbf{P}}^i)(\Delta t\ \mathbf{N}^{n+1/2-i}))$
(3)	$\widetilde{\mathbf{P}}^n \mathbf{G}p^{-1/2} - (\mathbf{I} - \widetilde{\mathbf{P}}) \sum \widetilde{\mathbf{P}}^{i-1} \Delta t\ \mathbf{N}^{n+1/2-i}$
(4)	$-(\mathbf{I} - \widetilde{\mathbf{P}})(\Delta t\ \mathbf{N}^{n-1/2})$

Table 2: $\Delta t\ \mathbf{G}p^{n-1/2}$ in terms of $\mathbf{U}^0$, $\mathbf{G}p^{-1/2}$, and $\mathbf{N}$. All sums are from $i = 1$ to n unless otherwise noted.

tests we have found that because the pressure from the first projection using version (1) is a good first guess for the pressure which would result from version (4), one can algebraically reformulate the second projection to solve for the difference between these two pressures rather than for the new pressure itself. It is then only necessary to approximately solve (e.g. to require that the iterative solver reduce the residual by only one order of magnitude) the second equation, resulting in little additional computational work. This new version has been successfully used to model incompressible axisymmetric flow with swirl in [16].

The expressions for projection (5) corresponding to those in Tables 1 and 2 are

$$\mathbf{U}^n = \widetilde{\mathbf{P}}^n \mathbf{U}^0 - \widetilde{\mathbf{P}}^n(\Delta t\ \mathbf{G}p^{-1/2}) - \widetilde{\mathbf{P}}(\Delta t\ \mathbf{N}^{n-1/2}) - \sum_{i=1}^{n-1} \widetilde{\mathbf{P}}^i(2\widetilde{\mathbf{P}} - \mathbf{I})(\Delta t\ \mathbf{N}^{n-1/2-i}),$$

$$\mathbf{G}p^{n-1/2} = (\mathbf{I} - \widetilde{\mathbf{P}})(\Delta t\ \mathbf{N}^{n-1/2}).$$

We note here that version (5) is fully second-order accurate for smooth problems; on the translating vortices problem the results are almost indistinguishable from those with version (2). For the random initial vorticity problem the divergence is shown in Figure 9, contrasted only with the data from versions (1) and (2). We see that the divergence for version (5) remains low in all cases; it is in fact always lower than that for version (2), and version (5) lacks the instability of version (1). For the simple steady problem, the curves for version (5) are indistinguishable from those for version (1).

Before performing a more detailed analysis of the projection version, we note that the results for each version can be expressed in a general form as

$$\mathbf{U}^n = \rho_n(\widetilde{\mathbf{P}})\mathbf{U}^0 - \Delta t\ \sum_{i=1}^{n} \alpha_i(\widetilde{\mathbf{P}})\mathbf{N}^{n+1/2-i} - \beta_n(\widetilde{\mathbf{P}})\mathbf{G}p^{-1/2}, \tag{4.1}$$

$$\Delta t\ \mathbf{G}p^{n-1/2} = -\Delta t\ (\mathbf{I} - \widetilde{\mathbf{P}})\mathbf{N}^{n-1/2} - \Delta t\ \sum_{i=2}^{n} \gamma_i(\widetilde{\mathbf{P}})\mathbf{N}^{n+1/2-i} + \gamma_n(\widetilde{\mathbf{P}})\mathbf{U}^0 - \Delta t\ \delta_n(\widetilde{\mathbf{P}})\mathbf{G}p^{-1/2}, \tag{4.2}$$

with the polynomial coefficients for each version and for an exact projection given in Table 3.

Performing a complete error analysis for each of these approximate schemes is not tractable. Instead, to characterize the effect of the "approximateness" of the approximate projection in greater detail, we will use the formulae in (4.1)-(4.2) to compare the solution found using the approximate projection to the solution of the same problem found using the corresponding exact discrete projection $\mathbf{P}$. If we denote by $(\mathbf{U}^n, \mathbf{G}p^{n-1/2})$ the solution with $\widetilde{\mathbf{P}}$ and $(\mathbf{V}^n, \mathbf{G}q^{n-1/2})$ the solution with $\mathbf{P}$, then

$$\mathbf{U}^n - \mathbf{V}^n = (\rho^n(\widetilde{\mathbf{P}}) - \mathbf{P})\mathbf{U}^0 - \Delta t\ \sum_{i=1}^{n} \alpha_i(\widetilde{\mathbf{P}})\mathbf{N}_U^{n+1/2-i} + \Delta t\ \sum_{i=1}^{n} \mathbf{P}\mathbf{N}_V^{n+1/2-i} - \Delta t\ \beta_n(\widetilde{\mathbf{P}})\mathbf{G}p^{-1/2}$$

and

$$\begin{aligned}\Delta t\ (\mathbf{G}p^{n-1/2} - \mathbf{G}q^{n-1/2}) \quad = \quad & -\Delta t\ (\mathbf{I} - \widetilde{\mathbf{P}})\mathbf{N}_U^{n-1/2} + \Delta t\ (\mathbf{I} - \mathbf{P})\mathbf{N}_V^{n-1/2} - \Delta t\ \sum_{i=2}^{n} \gamma_i(\widetilde{\mathbf{P}})\mathbf{N}_U^{n+1/2-i} \\ & + \gamma_n(\widetilde{\mathbf{P}})\mathbf{U}^0 - \Delta t\ \delta_n(\widetilde{\mathbf{P}})\mathbf{G}p^{-1/2},\end{aligned}$$

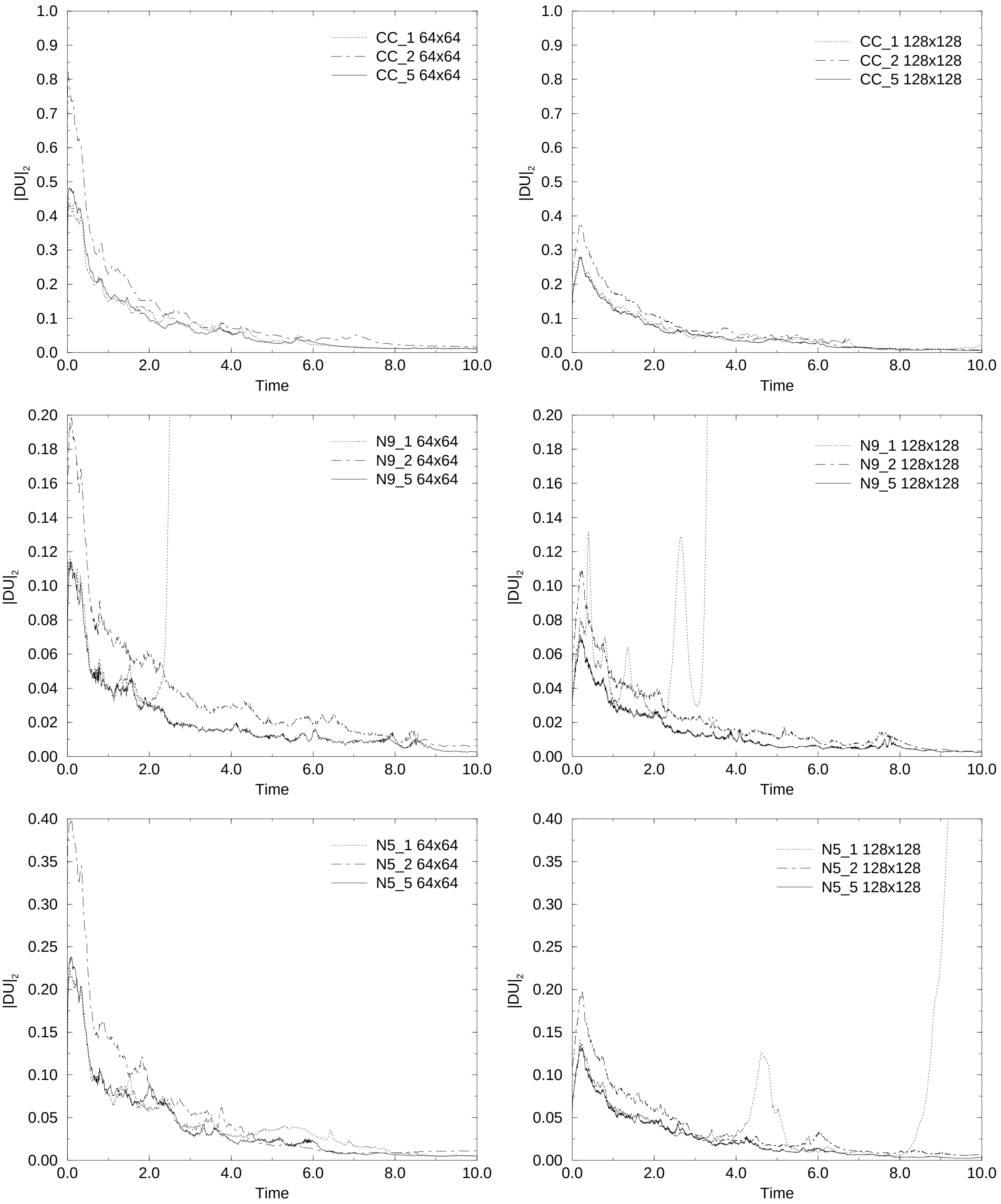

Figure 9: L2 norm of $\mathbf{DU}$ from $t = 0$ to 10 for the random initial vorticity problem at two different resolutions. Only approximate projection versions (1), (2) and (5) are shown.

Version	ρ_n	α_i	β_n	γ_i	δ_n
Exact	1	$\mathbf{P}$	0	0	0
(1)	$\mathbf{Q}_\alpha^n$	$\mathbf{Q}_\alpha^i$	$\mathbf{Q}_\beta^n$	$\mathbf{Q}_\gamma^i$	$\mathbf{Q}_\delta^n$
(2)	$\widetilde{\mathbf{P}}^n$	$\widetilde{\mathbf{P}}^i$	0	$\widetilde{\mathbf{P}}^{i-1} - \widetilde{\mathbf{P}}^i$	0
(3)	1	$\widetilde{\mathbf{P}}^i$	$\sum_{i=1}^n \widetilde{\mathbf{P}}^i$	$\widetilde{\mathbf{P}}^{i-1} - \widetilde{\mathbf{P}}^i$	$\widetilde{\mathbf{P}}^n$
(4)	1	$\widetilde{\mathbf{P}}$	0	0	0
(5)	$\widetilde{\mathbf{P}}^n$	$2\widetilde{\mathbf{P}}^{i+1} - \widetilde{\mathbf{P}}^i$	$\widetilde{\mathbf{P}}^n$	0	0

Table 3: Coefficients for each version of the approximate projection and for an exact projection.

where $\mathbf{N}_U$ and $\mathbf{N}_V$ denote evaluation of the advective terms with $(\mathbf{U}^n, \mathbf{G}p^{n-1/2})$ and $(\mathbf{V}^n, \mathbf{G}q^{n-1/2})$, respectively.

If we rewrite these expressions, adding and subtracting terms involving $\mathbf{P}\mathbf{N}_U^{n+1/2-i}$ to the equations we obtain

$$\begin{aligned}
\mathbf{U}^n - \mathbf{V}^n \quad = \quad & (\rho^n(\widetilde{\mathbf{P}}) - \mathbf{P})\mathbf{U}^0 - \Delta t \sum_{i=1}^{n} (\alpha_i(\widetilde{\mathbf{P}}) - \mathbf{P})\mathbf{N}_U^{n+1/2-i} - \Delta t \sum_{i=1}^{n} \mathbf{P}(\mathbf{N}_U^{n+1/2-i} - \mathbf{N}_V^{n+1/2-i}) \\
& -\Delta t \; \beta_n(\widetilde{\mathbf{P}})\mathbf{G}p^{-1/2}
\end{aligned}$$

and

$$\begin{aligned}
\Delta t \; (\mathbf{G}p^{n-1/2} - \mathbf{G}q^{n-1/2}) \quad = \quad & -\Delta t \; (\mathbf{P} - \widetilde{\mathbf{P}})\mathbf{N}_U^{n-1/2} - \Delta t \; (\mathbf{I} - \mathbf{P})(\mathbf{N}_U^{n-1/2} - \mathbf{N}_V^{n-1/2}) \\
& -\Delta t \sum_{i=2}^{n} \gamma_i(\widetilde{\mathbf{P}})\mathbf{N}_U^{n+1/2-i} + \gamma_n(\widetilde{\mathbf{P}})\mathbf{U}^0 - \Delta t \; \delta_n(\widetilde{\mathbf{P}})\mathbf{G}p^{-1/2},
\end{aligned}$$

If we now take norms and use the fact that $||\mathbf{P}|| = 1$ and $||\mathbf{I} - \mathbf{P}|| = 1$ we obtain

$$||\mathbf{U}^n - \mathbf{V}^n|| \quad \leq \quad ||(\rho^n(\widetilde{\mathbf{P}}) - \mathbf{P})\mathbf{U}^0|| + \Delta t \sum_{i=1}^{n} ||(\alpha_i(\widetilde{\mathbf{P}}) - \mathbf{P})\mathbf{N}_U^{n+1/2-i}|| \qquad (4.3)$$

$$+\Delta t\ \sum_{i=1}^{n} ||\mathbf{N}_U^{n+1/2-i} - \mathbf{N}_V^{n+1/2-i}|| + \Delta t\ ||\beta_n(\widetilde{\mathbf{P}})\mathbf{G}p^{-1/2}||$$

and

$$\begin{aligned}\Delta t\ ||\mathbf{G}p^{n-1/2} - \mathbf{G}q^{n-1/2}|| \ \leq\ & \Delta t\ ||(\mathbf{P} - \widetilde{\mathbf{P}})\mathbf{N}_U^{n-1/2}|| + \Delta t\ ||\mathbf{N}_U^{n-1/2} - \mathbf{N}_V^{n-1/2}|| \ + \\ & \Delta t\ \sum_{i=2}^{n} ||\gamma_i(\widetilde{\mathbf{P}})|N_U^{n+1/2-i}|| + ||\gamma_n(\widetilde{\mathbf{P}})|U^0|| + \Delta t\ ||\delta_n(\widetilde{\mathbf{P}})\mathbf{G}p^{-1/2}||. \end{aligned} \tag{4.4}$$

For the methods considered here $\mathbf{N}_U$ depends on $\mathbf{U}$ and $\mathbf{G}p$ smoothly, likewise $\mathbf{N}_V$ depends on $\mathbf{V}$ and $\mathbf{G}q$ smoothly, so we can assume $||\mathbf{N}_U - \mathbf{N}_V||$ terms are small and can be absorbed into the left hand side of the equation with the introduction of a constant multiplier C on the right hand side. With that assumption, summing (4.3) and (4.4) over n yields

$$\begin{aligned}\sum_{n=1}^{N}\{||\mathbf{U}^n - \mathbf{V}^n|| \ + \ & \Delta t\ ||\mathbf{G}p^{n-1/2} - \mathbf{G}q^{n-1/2}||\} \leq C\sum_{n=1}^{N}\Big\{||\rho^n(\widetilde{\mathbf{P}}) - \mathbf{P})\mathbf{U}^0|| \ + \\ & \Delta t\ \sum_{i=1}^{n} ||(\alpha_i(\widetilde{\mathbf{P}}) - \mathbf{P})\mathbf{N}_U^{n+1/2-i}|| + \Delta t\ ||\beta_n(\widetilde{\mathbf{P}})\mathbf{G}p^{-1/2}|| + ||\gamma_n(\widetilde{\mathbf{P}})\mathbf{U}^0|| \ + \\ & \Delta t\ ||\delta_n(\widetilde{\mathbf{P}})\mathbf{G}p^{-1/2}|| + \Delta t\ ||(\mathbf{P} - \widetilde{\mathbf{P}})\mathbf{N}_U^{n-1/2}|| + \Delta t\ \sum_{i=2}^{n} ||\gamma_i(\widetilde{\mathbf{P}})\mathbf{N}_U^{n+1/2-i}||\Big\}\end{aligned} \tag{4.5}$$

From (4.5) we can exactly identify the polynomial expressions which contribute to the error due to the approximateness of the projection; these terms will be examined further in the next section.

Before examining the spatial structure of the different approximate projection schemes, we note that the derivation presented here also provides a characterization of the divergence of the solution of the approximate projection solution. If we apply $\mathbf{D}$ to (4.1) we obtain

$$\mathbf{D}\mathbf{U}^n \ = \ \mathbf{D}\rho^n(\widetilde{\mathbf{P}})\mathbf{U}^0 - \Delta t\ \sum_{i=1}^{n} \mathbf{D}\alpha_i(\widetilde{\mathbf{P}})\mathbf{N}_U^{n+1/2-i} - \Delta t\ \mathbf{D}\beta_n(\widetilde{\mathbf{P}})\mathbf{G}p^{-1/2}$$

Thus, the structure of the spatial operators described below also provides a characterization of the divergence. Furthermore, since $\widetilde{\mathbf{P}}$ and $\mathbf{P}$ do not change discretely divergence-free fields, the error terms in the estimate (4.5) are discrete gradients. This explains the correspondence between the quality of the computational results and the behavior of the discrete divergence of the solution.

5 Spatial Analysis of the Projection

The temporal analysis of the previous section provides a basic framework for understanding the behavior of approximate projection schemes. The details of this behavior depend on the details of the spatial structure of the approximate projections. In this section we will analyze that behavior for the **N5, N9** and **C5** approximate projections. In particular, we will look at how well the polynomials of $\widetilde{\mathbf{P}}$ that characterize the approximate projections approximate the corresponding exact discrete projection.

Before looking at the behavior of the approximate projections, however, we first need to characterize the structure of the corresponding exact discrete projection, $\mathbf{I} - \mathbf{G}(\mathbf{DG})^{-1}\mathbf{D}$. As noted earlier, the difficulties associated with using these exact discrete projections arise from the (locally) decoupled stencils associated with $\mathbf{DG}$. This local decoupling is related to the presence of elements in the kernel of $\mathbf{G}$ other than constants. In two dimensions, for the nodal scheme $dim\ ker\ \mathbf{G} = 2$ and for the cell-centered scheme $dim\ ker\ \mathbf{G} = 4$. For each of these methods one of these elements corresponds to constants and the other modes are spurious. For the nodal scheme this additional mode corresponds to the Nyquist frequency in both directions. This mode is also in $ker\ \mathbf{G}$ for the cell-centered scheme, as well as vertical and horizontal "stripe" modes corresponding to the Nyquist frequency in one component and constant in the other. These modes can be seen in Figure 5.

To characterize the projections we will look at their Fourier behavior. After the Fourier transform, the projection has the form of a 2x2 matrix for each wave number. As noted above, discretely divergence-free vector fields are unchanged by both the exact discrete and the approximate projections, thus both the exact discrete and approximate versions share an eigenvalue of 1 with a common eigenvector. To characterize the behavior we can then focus on the other eigenvalue, λ_{min}. For $\mathbf{P}$, $\lambda_{min} = 0$ except for wave numbers corresponding to elements in $ker\ \mathbf{G}$. In Figure 10 we show λ_{min} for the exact projection operator, $\mathbf{P}$, and for the **N9, N5** and **C5** approximate projection operators, $\widetilde{\mathbf{P}}$. In Figures 10-14 the center of each plot corresponds to the Nyquist frequency in both directions with constants at the corner. (The peak at constants has been suppressed.) The analogous characterization for the three-dimensional versions of these operators is presented in Appendix B.

In each case we see that λ_{min} for the approximate projection operator has a smooth peak near the elements of $ker\ \mathbf{G}$ for the corresponding exact discrete projection. Thus, because of additional elements in $ker\ \mathbf{G}$ the cell-centered discretization broadens the range over which the approximation is a poor one. We also note that the eigenvalue structure of the five-point nodal projection is similar to that of the nine-point nodal only with a slightly wider distribution. A key property of each discretization is that $\widetilde{\mathbf{P}}^n \to \mathbf{P}$ as $n \to \infty$.

From the characterization of the approximate projection in Figure 10 we can already explain the poor performance of versions (3) and (4) of the approximate projection method. In version (4), $\alpha_i(\widetilde{\mathbf{P}}) = \widetilde{\mathbf{P}}$ and so at each time step $\mathbf{U}$ accumulates a portion of the discrete gradient component of $\mathbf{N}$, resulting in an error that builds over time. By contrast, for version (2), $\alpha_i(\widetilde{\mathbf{P}}) = \widetilde{\mathbf{P}}^i$, so that the contributions from any fixed time converge to the correct contribution as n increases, because $\widetilde{\mathbf{P}}^n \to \mathbf{P}$.

The difficulty with version (3), on the other hand, is caused by a residual imprint of pressure as characterized by the β_n. Recall that for version (3), $\beta_n = \sum_i \widetilde{\mathbf{P}}^i$. For each eigenvalue we can write

$$\widetilde{\mathbf{P}}(\mathbf{G}\phi(\xi)) = \lambda(\xi)\mathbf{G}\phi(\xi); \quad 0 < \lambda < 1;$$

then for version (3)

$$\beta_n(\widetilde{\mathbf{P}})\mathbf{G}(\xi) \equiv (\widetilde{\mathbf{P}} + \widetilde{\mathbf{P}}^2 + ... + \widetilde{\mathbf{P}}^n)\mathbf{G}\phi(\xi) \to \frac{\lambda}{\lambda - 1}\mathbf{G}\phi(\xi),$$

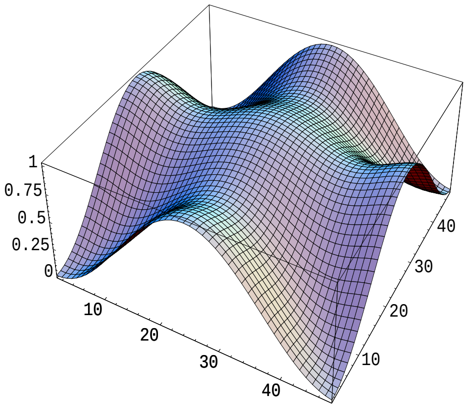

(a) λ_{min} for **C5**.

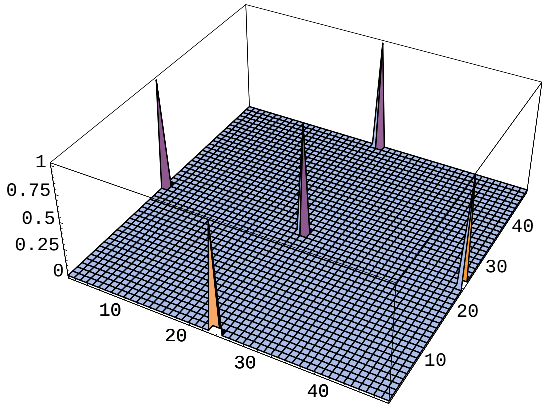

(b) λ_{min} for **C_EX**.

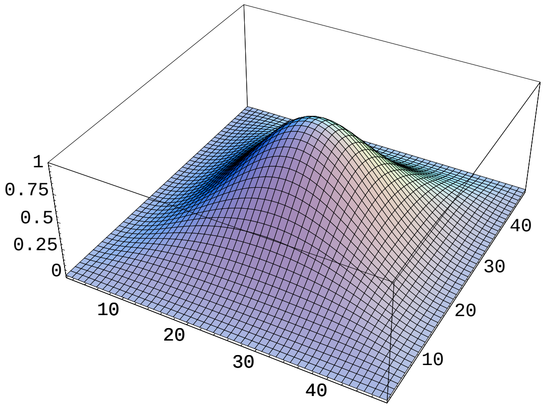

(c) λ_{min} for **N9**.

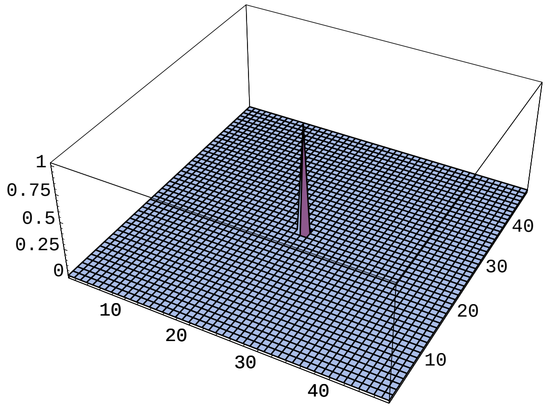

(d) λ_{min} for **N_EX**.

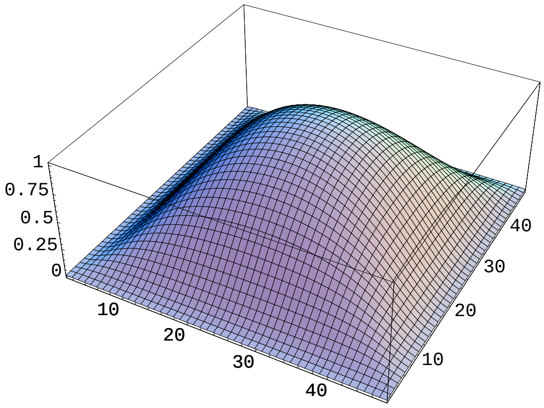

(e) λ_{min} for **N5**.

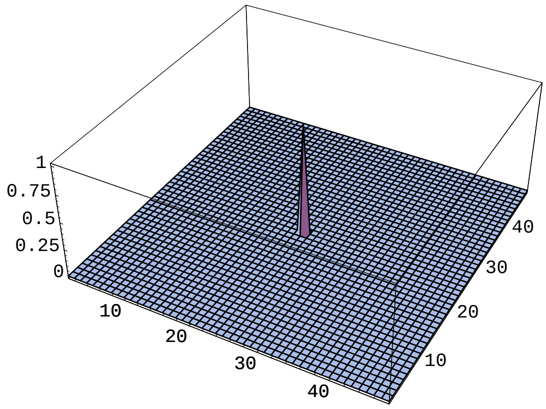

(f) λ_{min} for **N_EX**.

Figure 10: Smallest eigenvalue λ_{min} of the approximate and exact projections.

so that the pressure gradient terms in $\mathbf{U}$ that are annihilated by the exact discrete projection asymptote to a non-negligible error in $\mathbf{U}$ with an approximate projection. By contrast, we note that this type of term is absent for version (2) (i.e. $\beta_n = 0$) which is otherwise similar in structure to version (3).

To characterize the other versions of the approximate projection we look at the α_i in more detail. For each of the other three versions ((1), (2) and (5)) of the approximate projection, the lowest power of $\widetilde{\mathbf{P}}$ in α_i increases with i. Furthermore, the coefficients in α_i sum to 1. Therefore, for each version $\alpha_i(\widetilde{\mathbf{P}}) \to \mathbf{P}$ as $i \to \infty$. To obtain a more detailed comparison we need to look at the behavior of the α_i for small i.

For each version $\alpha_1(\widetilde{\mathbf{P}}) = \widetilde{\mathbf{P}}$ which is described above and illustrated in Figure 10. For the next two terms in the expressions, for version (1), $\alpha_2 = 2\widetilde{\mathbf{P}}^2 - \widetilde{\mathbf{P}}$, $\alpha_3 = 4\widetilde{\mathbf{P}}^3 - 3\widetilde{\mathbf{P}}^2$; for version (2), $\alpha_2 = \widetilde{\mathbf{P}}^2, \alpha_3 = \widetilde{\mathbf{P}}^3$; and for version (5), $\alpha_2 = 2\widetilde{\mathbf{P}}^2 - \widetilde{\mathbf{P}}, \alpha_3 = 2\widetilde{\mathbf{P}}^3 - \widetilde{\mathbf{P}}^2$. In Figure 11 we plot α_2 for **C5_1, C5_2** and **C5_5**, and **N9_1, N9_2** and **N9_5**. (The **N5** results are similar to the **N9** results only somewhat wider.) Figure 12 shows the analogous results for α_3.

For α_2, we note that for versions (1) and (5) there is a narrower peak than for version (2) near the frequencies that are in *ker* $\mathbf{G}$, with some small negative values at intermediate frequencies. Overall it is smaller in an L^2 integral sense. A similar pattern is observed for the α_3's. For version (2), the peak is fairly broad but the values are between 0 and 1. For version (5), the peak is narrow and there is a small region where the values are slightly negative ($\lambda_{min} > -.04$). For version (1), the peak near the *ker* $\mathbf{G}$ elements is sharpest but there are fairly large negative values ($\lambda_{min} = -.25$). Although version (1) is the smallest in an integral sense, the negative values can introduce perturbations into the solution which may be a contributing factor to the non-robustness of version (1).

There are two other potential sources for the behavior of version (1). As with version (3), version (1) contains a residual contribution from the pressure gradient (i.e. $\beta_n \neq 0$). For version (2) there is no such term; for version (5) this term is $\widetilde{\mathbf{P}}^n$ which goes to zero on the range of $\mathbf{G}$ as $n \to \infty$. For version (1), this behavior is characterized by the behavior of the $\mathbf{Q}_\beta$'s defined in Section 5. In Figure 13 we plot the functions β_2, β_3 and β_4 for **N9**. For comparison we also plot the corresponding functions for version (3). Unlike the operators for version (3) which asymptotically converge to nonzero values, the operators described here do not converge to zero for any fixed frequency except those near elements in *ker* G. However, the peak value near elements in *ker* $\mathbf{G}$ is n for the β_n for version (1), just as in version (3) but with a narrower peak. This growth in residual influence of $\mathbf{G}p^{-1/2}$ also has the potential for contribution to the non-robust behavior of version (1).

The final issue regarding the spatial structure associated with the approximate projection versions concerns the error in $\mathbf{G}p^{n-1/2}$ associated with the $\mathbf{N}$'s. For all versions the leading error term looks like $\mathbf{P} - \widetilde{\mathbf{P}}$, which we have already examined. For versions (4) and (5) there are no other terms. In Figure 14 we compare γ_2, γ_3 and γ_4 for versions (2) and (3) with the corresponding operators for version (1), again for **N9**. Here we see that the operators corresponding to version (1) are larger in magnitude than their counterparts in versions (2) and (3). They also attain non-negligible negative values at intermediate frequencies.

To summarize the findings, we first note that the unacceptable performance of versions (3)

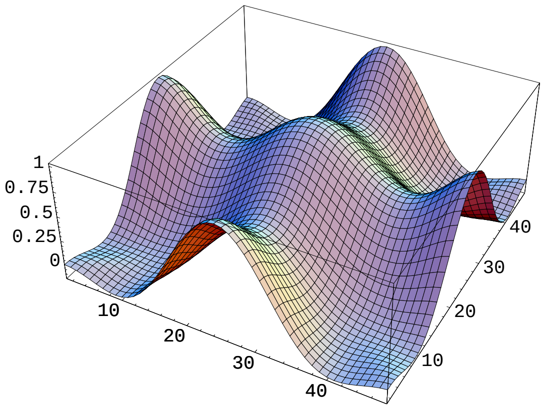

(a) α_2 for **C5_1, C5_5**.

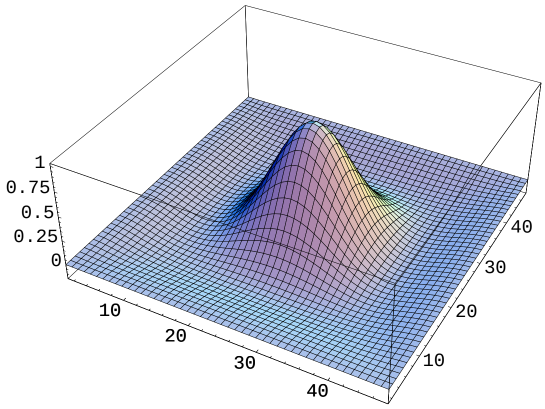

(b) α_2 for **N9_1, N9_5**.

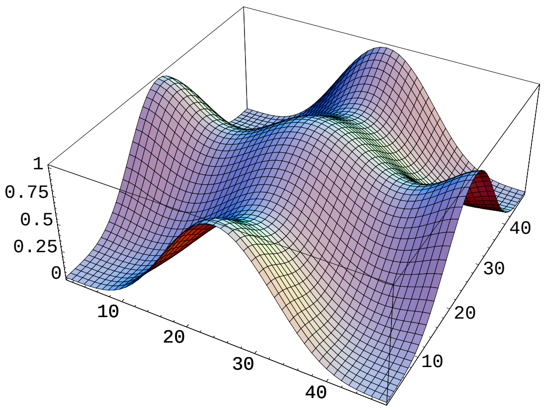

(c) α_2 for **C5_2**.

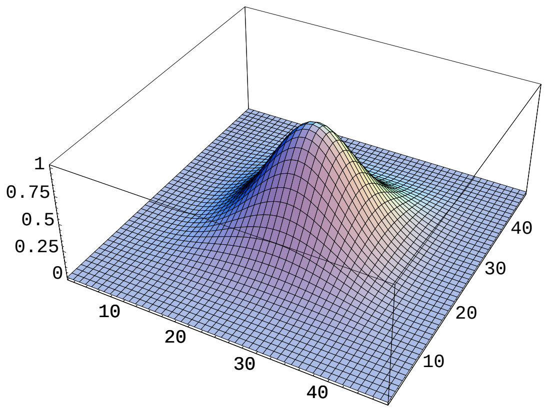

(d) α_2 for **N9_2**.

Figure 11: α_2 for versions (1),(2) and (5) of the approximate projections.

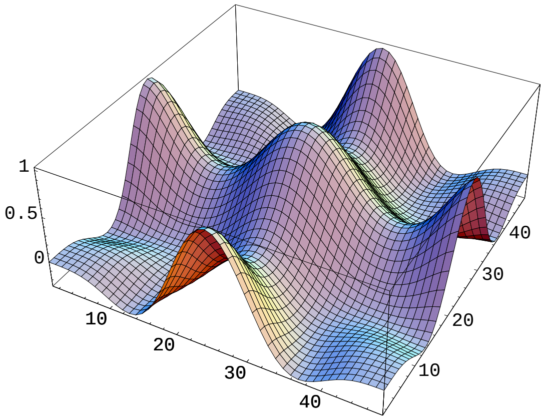

(a) α_3 for **C5_1**.

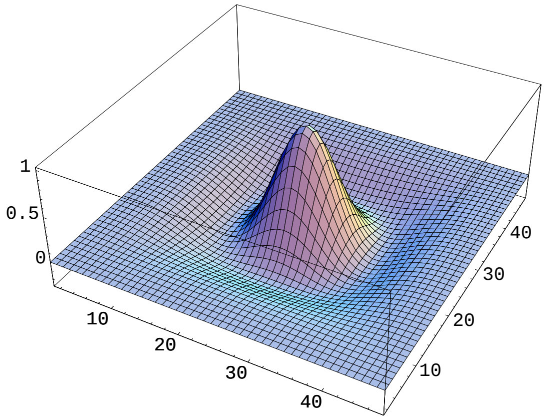

(b) α_3 for **N9_1**.

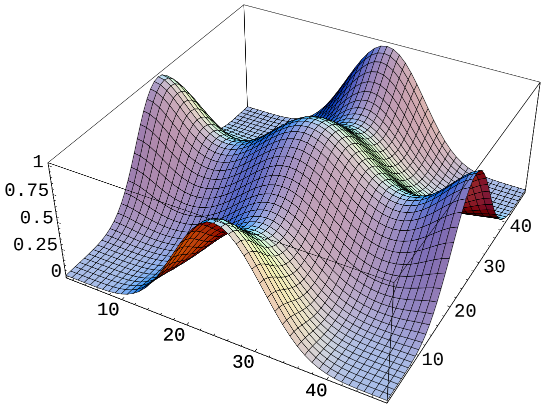

(c) α_3 for **C5_2**.

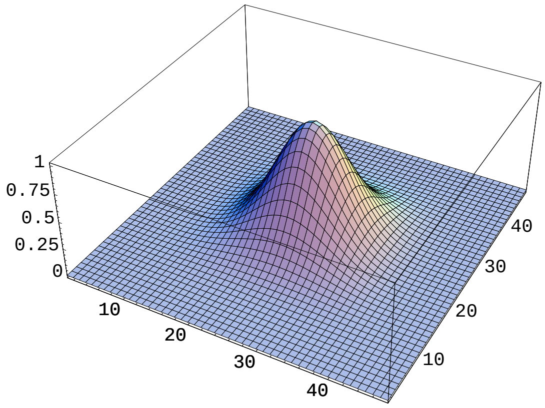

(d) α_3 for **N9_2**.

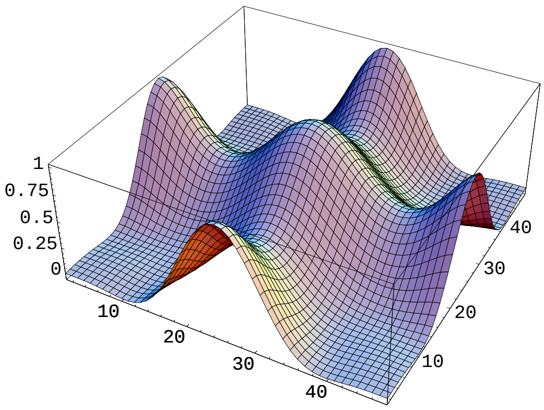

(e) α_3 for **C5_5**.

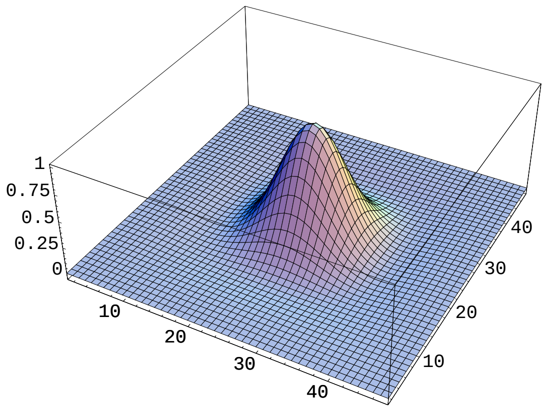

(f) α_3 for **N9_5**.

Figure 12: α_3 for versions (1),(2) and (5) of the approximate projections.

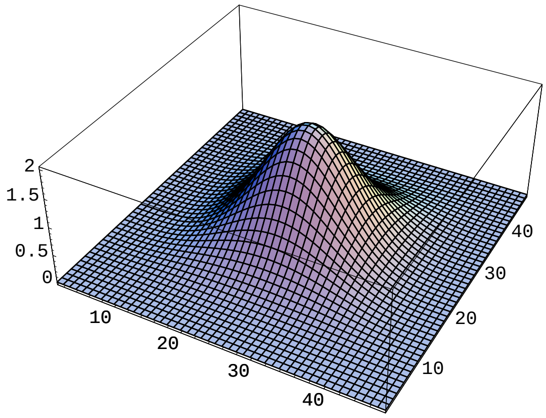

(a) β_2 for **N9_1**.

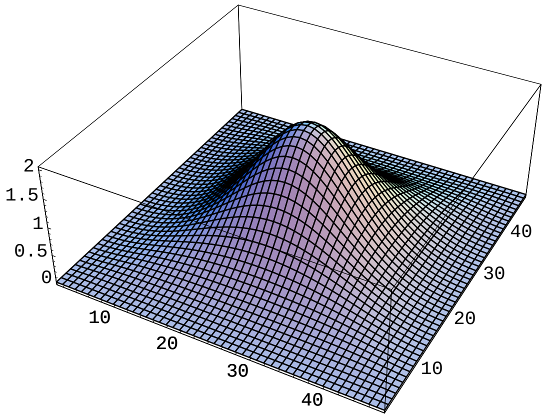

(b) β_2 for **N9_3**.

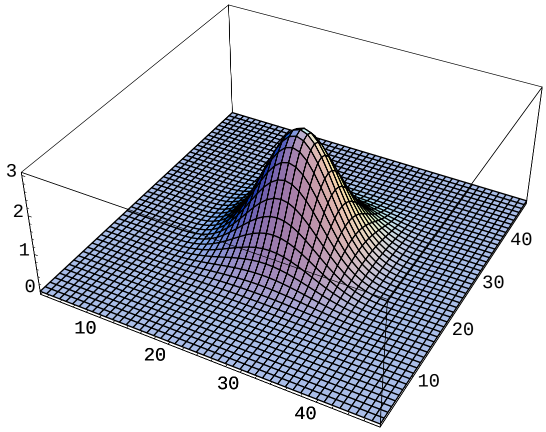

(c) β_3 for **N9_1**.

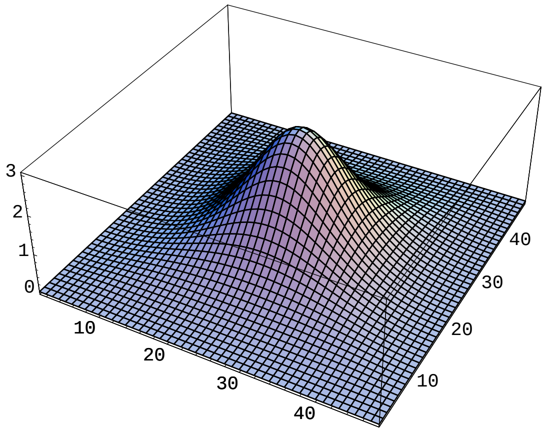

(b) β_3 for **N9_3**.

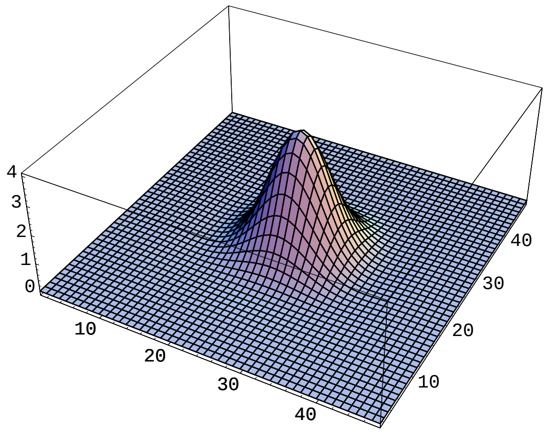

(e) β_4 for **N9_1**.

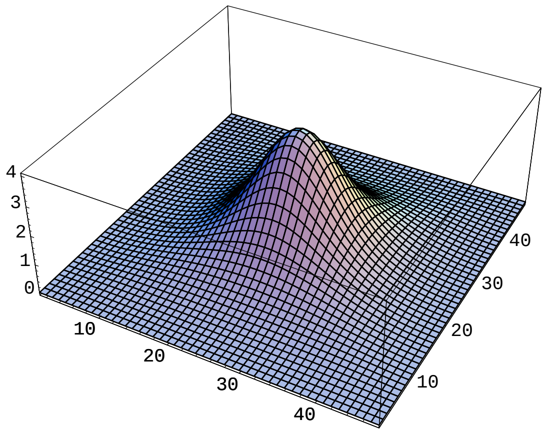

(f) β_4 for **N9_3**.

Figure 13: β_2, β_3, and β_4 for the **N9_1** and **N9_3** approximate projections.

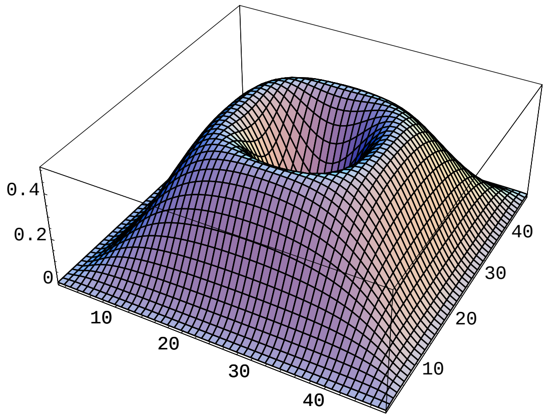

(a) γ_2 for **N9_1**.

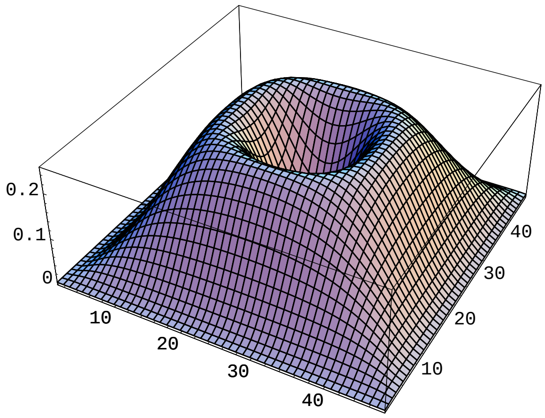

(b) γ_2 for **N9_3**.

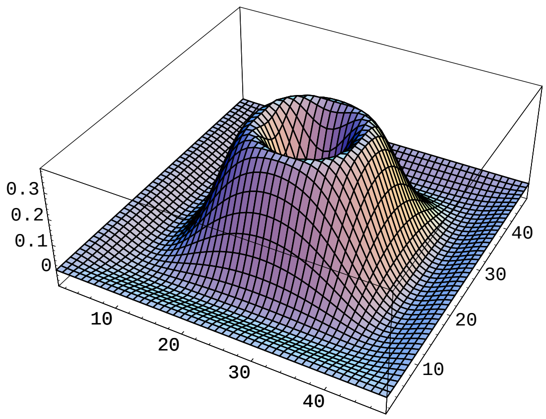

(c) γ_3 for **N9_1**.

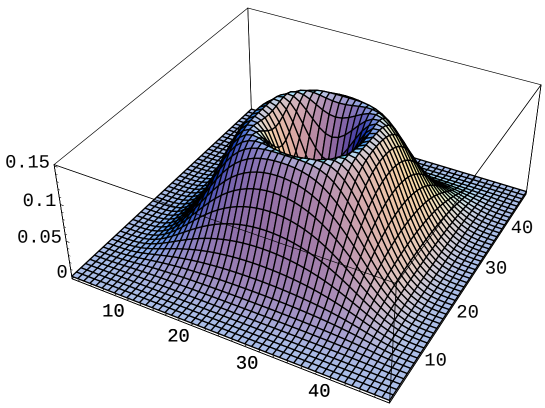

(d) γ_3 for **N9_3**.

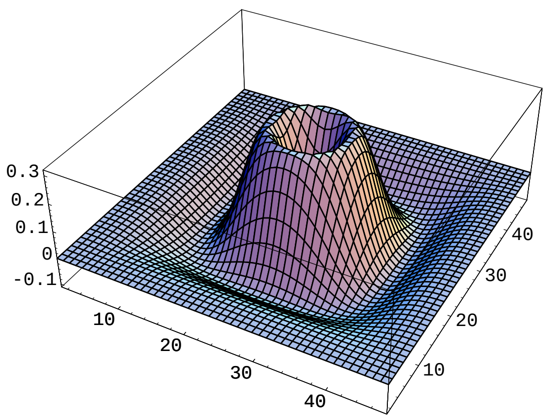

(e) γ_4 for **N9_1**.

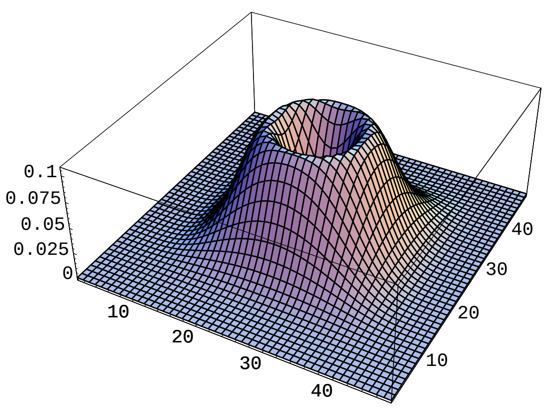

(f) γ_4 for **N9_3**.

Figure 14: γ_2, γ_3, and γ_4 for the **N9_1** and **N9_3** approximate projections.

and (4) can be related to an imprint of the old pressure gradients and a failure to damp the gradient components of the advection terms, respectively. We have identified three features of version (1) which may contribute to its lack of robustness. The first is the oscillatory nature of the α_i; however, this is a relatively small effect and probably plays a negligible role in determining the overall behavior. The other two features, a growing imprint of the old pressure gradient on $\mathbf{U}$ given by the β_i's combined with the errors introduced into $\mathbf{G}p$ from the advection terms specified by the γ_i's provide a mechanism for feeding back oscillatory behavior into the solution.

6 Advection-Projection Coupling

As we can see from the numerical results and the analysis, the nature of the difficulties for versions (3) and (4) differs from that of version (1). This is evident as well in further numerical testing. Here we perform two additional numerical experiments with the random initial vorticity problem. In the first we halve the timestep in each calculation by reducing the CFL number from 0.9 to 0.45 to examine the effect on the solution. In the left column of Figure 15, for resolution 64^2, we see that the results from versions (3) and (4) are essentially unchanged but the results from versions (1) are markedly improved (i.e. lower divergence) relative to the results shown in Figure 7. Version (1) has also been rerun for resolution 128^2, with the same improvement.

Our second experiment is to modify the predictor so that the coupling between the pressure gradient $\mathbf{G}p^{n-1/2}$ and the advective update term $\mathbf{N}^{n+1/2}$ is reduced, by MAC-projecting the advected velocities as well as the advection velocities in the predictor step. This modification is described in more detail in Appendix A. The results for the same cases as above are shown in the right column of Figure 15; here the results of versions (3) and (4) are worsened (in the sense that the divergence is larger) but the divergence from version (1) is again noticeably lower, again compared to Figure 7. This experiment was run at CFL = 0.9.

The results in this section suggest that the poor results obtained with versions (3) and (4), and the acceptable results of versions (2) and (5), are independent of the choice of advection scheme. By contrast, the behavior of version (1) for inviscid flow is intimately coupled to the details of the particular advection method.

7 Conclusions and Future Work

When adopting an approximate projection formulation in which the projection operator does not exactly enforce a discrete divergence condition on the velocity field, there are several options for which vector field to project. In this paper we have explored these options computationally and developed an analytical framework that explains the computational results. The results show that projecting the velocity field rather than the velocity increment is necessary to produce acceptable results. We also find that projecting $\frac{\mathbf{U}^{*,n+1}}{\Delta t}$ (version (1)) can produce a lower divergence in the computed solution than projecting $\frac{\mathbf{U}^{*,n+1}}{\Delta t} + \mathbf{G}p^{n-1/2}$ (version (2)); however, it is not as robust as version (2) which always produces acceptable results.

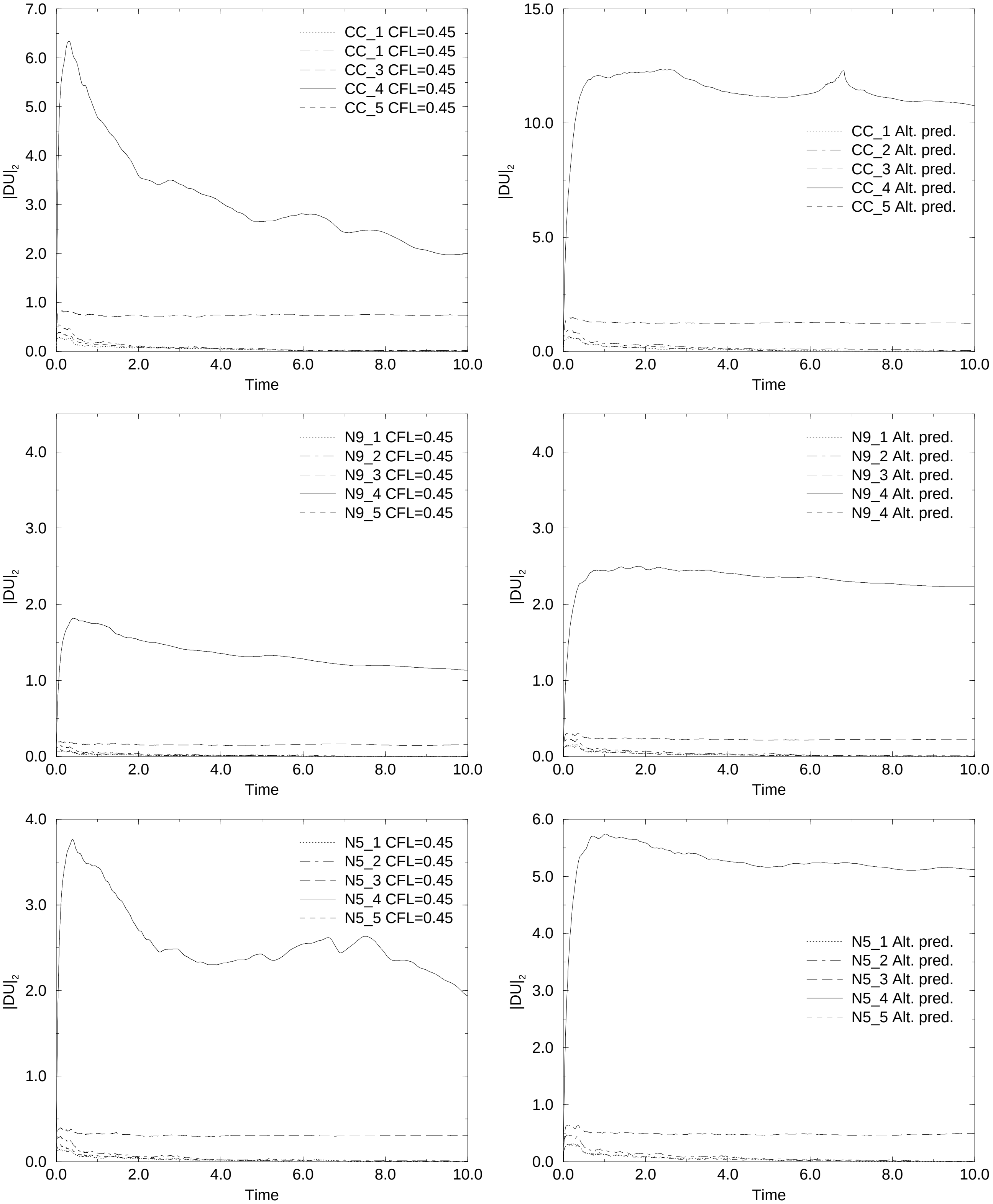

Figure 15: L2 norm of **DU** from $t = 0$ to 10 with CFL = 0.45 (left column), or the alternate predictor (right column).

We have also introduced a new approximate projection formulation based on projecting $\frac{\mathbf{U}^{*,n+1}}{\Delta t}$ to update $\mathbf{U}^{n+1}$ while projecting $\frac{\mathbf{U}^{*,n+1}-\mathbf{U}^{n}}{\Delta t} + \mathbf{G}p^{n-1/2}$ as an iterative correction to update p. The new formulation produces results similar to version (1) when version (1) is successful and exhibits the same robustness as version (2).

In the next paper we will present the extension of the analysis to viscous flows. Although we have seen here that minor variations in the advection step can be exploited to obtain better results with version (1), when viscosity is introduced the poor behavior of version (1) cannot be salvaged. Further issues and future work will include the extension of the analysis for variable density flows, adaptive mesh calculations with subcycling in time, and low Mach number flows with non-zero divergence constraints.

Appendix A: The Predictor / Corrector Step

In this section we first describe the construction of the advective update $\mathbf{N}^{n+1/2}$ used in our original tests; then we discuss the modifications as discussed in Section 6.

In the predictor we first extrapolate the normal velocities to cell faces at $t^{n+1/2}$. For face $(i+1/2, j)$ this gives

$$\tilde{u}^{L,n+1/2}_{i+1/2,j} = u^n_{i,j} + (\frac{\Delta x}{2} - u^n_{i,j}\frac{\Delta t}{2})(u^{n,lim}_x)_{i,j} + \frac{\Delta t}{2}(-(\widehat{vu_y})_{i,j} - (G_x p)^{n-1/2}_{i,j})$$

extrapolated from (i,j), and

$$\tilde{u}^{R,n+1/2}_{i+1/2,j} = u^n_{i+1,j} - (\frac{\Delta x}{2} + u^n_{i+1,j}\frac{\Delta t}{2})(u^{n,lim}_x)_{i+1,j} + \frac{\Delta t}{2}(-(\widehat{vu_y})_{i+1,j} - (G_x p)^{n-1/2}_{i+1,j})$$

extrapolated from $(i+1,j)$. Here the first derivatives normal to the face (in this case $u^{n,lim}_x$) are evaluated using a monotonicity-limited fourth-order slope approximation [6] (unless specified to use unlimited slopes), and the the transverse derivative terms ($\widehat{vu_y}$ in this case) are evaluated exactly as in [1]. $\mathbf{G} = (G_x, G_y)$ is a discretization of the gradient operator. For a nodal pressure field,

$$\begin{aligned}
(G_x p)_{i,j} &= \frac{1}{4\Delta x}(p_{i+1/2,j+1/2} + p_{i+1/2,j-1/2} - p_{i-1/2,j+1/2} - p_{i-1/2,j-1/2}),\\
(G_y p)_{i,j} &= \frac{1}{4\Delta y}(p_{i+1/2,j+1/2} + p_{i-1/2,j+1/2} - p_{i+1/2,j-1/2} - p_{i-1/2,j-1/2}).
\end{aligned}$$

For a cell-centered pressure field,

$$\begin{aligned}
(G_x p)_{i,j} &= \frac{1}{2\Delta x}(p_{i+1,j} - p_{i-1,j}),\\
(G_y p)_{i,j} &= \frac{1}{2\Delta x}(p_{i,j+1} - p_{i,j-1}).
\end{aligned}$$

Analogous formulae are used to predict values for $\tilde{u}^{L/R,n+1/2}_{i-1/2,j}$, $\tilde{v}^{F/B,n+1/2}_{i,j+1/2}$, and $\tilde{v}^{F/B,n+1/2}_{i,j-1/2}$.

The normal velocity at each face is then determined by an upwinding procedure based on the states predicted from the cell centers on either side.

$$\tilde{u}^{n+1/2}_{i+1/2,j} = \begin{cases} \tilde{u}^{L,n+1/2} & \text{if } \tilde{u}^{L,n+1/2} > 0 \text{ and } \tilde{u}^{L,n+1/2} + \tilde{u}^{R,n+1/2} > 0 \\ 0 & \text{if } \tilde{u}^{L,n+1/2} \leq 0, \tilde{u}^{R,n+1/2} \geq 0 \text{ or } \tilde{u}^{L,n+1/2} + \tilde{u}^{R,n+1/2} = 0 \\ \tilde{u}^{R,n+1/2} & \text{if } \tilde{u}^{R,n+1/2} < 0 \text{ and } \tilde{u}^{L,n+1/2} + \tilde{u}^{R,n+1/2} < 0 \end{cases}$$

We follow a similar procedure to construct $\tilde{v}^{n+1/2}_{i,j+1/2}$.

In order to enforce the divergence-free condition on these edge-based velocities we now impose the MAC projection (see [4]). The equation

$$\mathbf{D}^{MAC}(\mathbf{G}^{MAC}\phi^{MAC}) = \mathbf{D}^{MAC}(\tilde{U}^{n+1/2})$$

is solved for ϕ^{MAC}, with homogeneous Neumann boundary conditions on all physical boundaries except for outflow, where ϕ^{MAC} is set to zero to enforce the "no tangential acceleration" criterion. Here

$$\mathbf{D}^{MAC}(\widetilde{U}^{n+1/2}) = \frac{\widetilde{u}^{n+1/2}_{i+1/2,j} - \widetilde{u}^{n+1/2}_{i-1/2,j}}{\Delta x} + \frac{\widetilde{v}^{n+1/2}_{i,j+1/2} - \widetilde{v}^{n+1/2}_{i,j-1/2}}{\Delta y}$$

and $\mathbf{G}^{MAC} = -(\mathbf{D}^{MAC})^T$ so that

$$(G_x^{MAC}\phi^{MAC})_{i+1/2,j} = \frac{(\phi^{MAC}_{i+1,j} - \phi^{MAC}_{i,j})}{\Delta x}, \quad (G_y^{MAC}\phi^{MAC})_{i,j+1/2} = \frac{(\phi^{MAC}_{i,j+1} - \phi^{MAC}_{i,j})}{\Delta x}.$$

The advection velocity U^{ADV} is then defined by

$$\begin{aligned}
u^{ADV}_{i+1/2,j} &= \widetilde{u}^{n+1/2}_{i+1/2,j} - (G_x^{MAC}\phi^{MAC}), \\
v^{ADV}_{i,j+1/2} &= \widetilde{v}^{n+1/2}_{i,j+1/2} - (G_y^{MAC}\phi^{MAC}).
\end{aligned}$$

At this point the tracing step from cell centers to edges is performed for both the normal and tangential velocity components exactly as above, except that the upwinding now depends on the MAC-projected advection velocity, i.e.,

$$\widetilde{U}_{i+1/2,j} = \begin{cases} \widetilde{U}^L & \text{if } u^{ADV}_{i+1/2,j} > 0 \\ 1/2(\widetilde{U}^L + \widetilde{U}^R) & \text{if } u^{ADV}_{i+1/2,j} = 0 \\ \widetilde{U}^R & \text{if } u^{ADV}_{i+1/2,j} < 0 \end{cases}$$

For the original advective term, we now define

$$\mathbf{N}_{i,j} = \frac{(u^{ADV}_{i+1/2,j}\widetilde{U}_{i+1/2,j} - u^{ADV}_{i-1/2,j}\widetilde{U}_{i-1/2,j})}{\Delta x} + \frac{(v^{ADV}_{i,j+1/2}\widetilde{U}_{i,j+1/2} - v^{ADV}_{i,j-1/2}\widetilde{U}_{i,j-1/2})}{\Delta y}$$

The modification of the predictor as described in Section 6 is the replacement of $\widetilde{U}$ by $\widetilde{\widetilde{U}} = (\widetilde{u}, \widetilde{v})$ in the above expression, where

$$\begin{aligned}
\widetilde{\widetilde{u}}_{i+1/2,j} &= u^{ADV}_{i,j+1/2} \\
\widetilde{\widetilde{u}}_{i,j+1/2} &= \widetilde{u}_{i,j+1/2} - \frac{1}{4\Delta x}(\phi^{MAC}_{i+1,j} + \phi^{MAC}_{i+1,j-1} - \phi^{MAC}_{i-1,j} - \phi^{MAC}_{i-1,j-1}), \\
\widetilde{\widetilde{v}}_{i+1/2,j} &= \widetilde{v}_{i+1/2,j} - \frac{1}{4\Delta x}(\phi^{MAC}_{i,j+1} + \phi^{MAC}_{i-1,j+1} - \phi^{MAC}_{i,j-1} - \phi^{MAC}_{i-1,j-1}) \\
\widetilde{\widetilde{v}}_{i,j+1/2} &= v^{ADV}_{i+1/2,j}.
\end{aligned}$$

Then

$$\mathbf{N}_{i,j} = \frac{(u^{ADV}_{i+1/2,j}\widetilde{\widetilde{U}}_{i+1/2,j} - u^{ADV}_{i-1/2,j}\widetilde{\widetilde{U}}_{i-1/2,j})}{\Delta x} + \frac{(v^{ADV}_{i,j+1/2}\widetilde{\widetilde{U}}_{i,j+1/2} - v^{ADV}_{i,j-1/2}\widetilde{\widetilde{U}}_{i,j-1/2})}{\Delta y}$$

Appendix B: Approximate Projection Operators in Three Dimensions

In this appendix we provide a characterization of the extension of the three different spatial approximate projections considered above to three space dimensions. We will refer to the seven-point cell-centered discretization as **C7**, the 21-point nodal discretization as **N21**, and the seven-point nodal discretization as **N7.** As before, the approximate projections do not alter discretely divergence-free vector fields. In three dimensions this means that the discrete projection operator is a 3×3 matrix for each frequency with two eigenvalues of 1. The other eigenvalue, λ_{min}, represents the degree to which gradients are damped by the projection. In Figure 16, we show two isosurfaces of this minimum eigenvalue for each discretization. As in the previous Fourier analysis pictures, the Nyquist frequency is in the center of the domain with constant modes appearing at the corners (with the corner spikes suppressed). The first contour is the $\lambda_{min} = 0.5$ surfaces. The region bounded by these surfaces extending toward the corners is the portion of the domain where $\lambda_{min} < 0.5$. The second contour corresponds to $\lambda_{min} = .9$. As in the two-dimensional case, this surface encloses the locus of nonconstant elements in *ker G*. For **C7** there are 8 elements in *ker* **G** while for **N7** and **N21** there is a one-dimensional family of elements. As a further characterization of these schemes, we can expand the smallest eigenvalue about the constant mode to obtain the behavior of the different approximations for low frequencies. In particular, for **C7** we obtain

$$\lambda_{min}(k_1, k_2, k_3) = \frac{(k_1^4 + k_1^4 + k4^2)}{2(k_1^2 + k_2^2 + k_3^2)},$$

for **N21** we obtain

$$\lambda_{min}(k_1, k_2, k_3) = \frac{(k_1^2 k_2^2 + k_1^2 k_3^2 + k_2^2 k_3^2)}{6(k_1^2 + k_2^2 + k_3^2)},$$

and for **N7** we obtain

$$\lambda_{min}(k_1, k_2, k_3) = \frac{(k_1^2 k_2^2 + k_1^2 k_3^2 + k_2^2 k_3^2)}{2(k_1^2 + k_2^2 + k_3^2)} \quad .$$

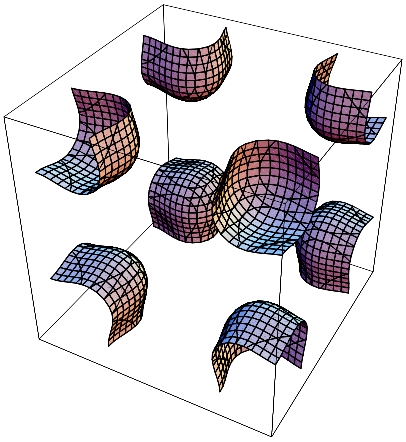

(a) $\lambda_{min} = 0.5$ for **C7**.

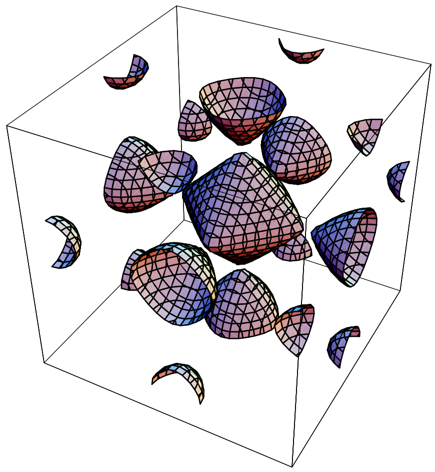

(b) $\lambda_{min} = 0.9$ for **C7**.

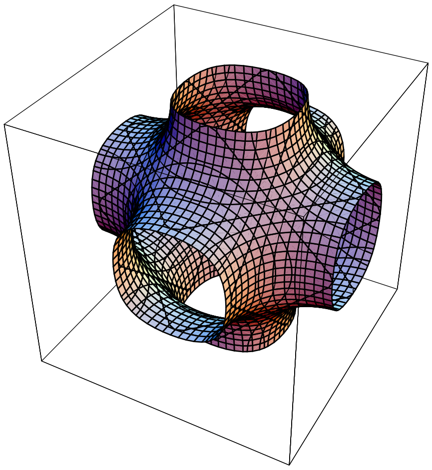

(c) $\lambda_{min} = 0.5$ for **N21**.

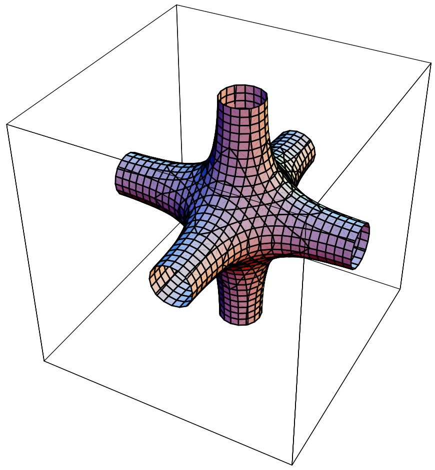

(d) $\lambda_{min} = 0.9$ for **N21**.

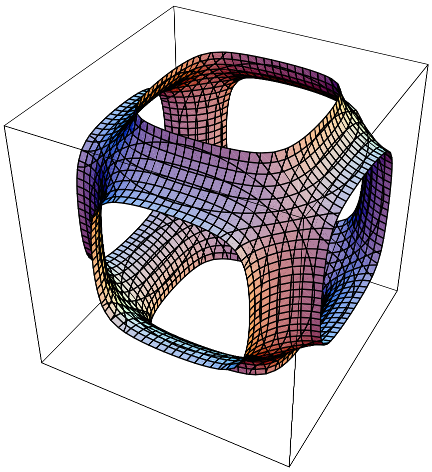

(e) $\lambda_{min} = 0.5$ for **N7**.

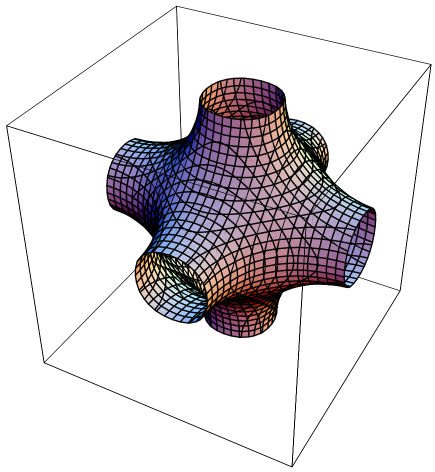

(f) $\lambda_{min} = 0.9$ for **N7**.

Figure 16: Isosurfaces of the smallest eigenvalue, λ_{min}, at values 0.5 and 0.9 of the 3D approximate projection operators.

References

[1] A. S. Almgren, J. B. Bell, P. Colella, L. H. Howell, and M. Welcome. A conservative adaptive projection method for the variable density incompressible Navier-Stokes equations. *J. Comput. Phys.*, 142:1–46, 1998.

[2] A. S. Almgren, J. B. Bell, and W. G. Szymczak. A numerical method for the incompressible Navier-Stokes equations based on an approximate projection. *SIAM J. Sci. Comput.*, 17(2), March 1996.

[3] J. B. Bell, P. Colella, and H. M. Glaz. A second-order projection method for viscous, incompressible flow. In *8th AIAA Computational Fluid Dynamics Conference*, Honolulu, June 9–11, 1987.

[4] J. B. Bell, P. Colella, and L. H. Howell. An efficient second-order projection method for viscous incompressible flow. In *10th AIAA Computational Fluid Dynamics Conference*, Honolulu, June 24–27, 1991.

[5] A. J. Chorin. Numerical solution of the Navier-Stokes equations. *Math. Comput.*, 22:745–762, October 1968.

[6] P. Colella. A direct Eulerian MUSCL scheme for gas dynamics. *SIAM Journal on Computing*, 6:104–117, January 1985.

[7] M. Fortin. Numerical solutions of the steady state Navier-Stokes equations. In *Numerical Methods in Fluid Dynamics*, 1972. AGARD-LS-48.

[8] L. H. Howell and J. B. Bell. An adaptive-mesh projection method for viscous incompressible flow. *SIAM J. Sci. Comput.*, 18:996–1013, 1997.

[9] G. Joyce and D. Montgomery. Negative temperature states for a two-dimensional guiding center plasma. *J. Plasma Phys.*, 10:107, 1973.

[10] M. F. Lai. *A Projection Method for Reacting Flow in the Zero Mach Number Limit.* PhD thesis, University of California at Berkeley, 1993.

[11] M. F. Lai, J. B. Bell, and P. Colella. A projection method for combustion in the zero Mach number limit. In *Proceedings of the Eleventh AIAA Computational Fluid Dynamics Conference*, pages 776–783, 1993.

[12] D. F. Martin. *An Adaptive Cell-Centered Projection Method for the Incompressible Euler Equations.* PhD thesis, University of California, Berkeley, 1998.

[13] J. C. McWiliams. The emergence of isolated coherent vortices in turbulent flow. *J. Fluid Mech.*, 146:21–43, 1984.

[14] M. L. Minion. A projection method for locally refined grids. *J. Comput. Phys.*, 127:158–178, 1996.

[15] D. Montgomery, X. Shan, and W. H. Matthaeus. Navier-Stokes relaxation to sinh-Poisson states at finite Reynolds numbers. *Phys. Fluids A*, 5:2207–2216, 1993.

[16] D. S. Nolan, A. S. Almgren, and J. B. Bell. High Reynolds number simulations of axisymmetric tornado-like vortices with adaptive mesh refinement. *J. Atmos. Sci.*, 1999. submitted for publication.

[17] R. B. Pember, A. S. Almgren, J. B. Bell, P. Colella, L. H. Howell, and M. Lai. A higher-order projection method for the simulation of unsteady turbulent nonpremixed combustion in an industrial burner. *Transport Phenomena in Combustion*, pages 1200–1211, 1996. Taylor and Francis.

[18] R. B. Pember, L. H. Howell, J. B. Bell, P. Colella, W. Y. Crutchfield, W. A. Fiveland, and J. P. Jessee. An adaptive projection method for unsteady, low-Mach number combustion. *Comb. Sci. Tech.*, to appear.

[19] W. J. Rider. Approximate projection methods for incompressible flow: Implementation, variants and robustness. Technical Report LA-UR-94-2000, LANL, 1994.

[20] W. J. Rider. Filtering non-solenoidal modes in numerical solutions of incompressible flows. *Intl. J. Num. Meths. in Fluids*, 28:789–814, 1998.

[21] D. E. Stevens, A. S. Almgren, and J. B. Bell. Adaptive simulations of trade cumulus convection. *Mon. Wea. Rev.*, submitted for publication.

[22] D. E. Stevens, J. B. Bell, A. S. Almgren, V. E. Beckner, and C. A. Rendleman. Small scale processes and entrainment in a stratocumulus marine boundary layer. *J. Atmos. Sci.*, to appear.

[23] R. Temam. Sur l'approximation de la solution des equations de Navier-Stokes par la methode des fractionaires ii. *Arch. Rational Mech. Anal.*, 33:377–385, 1969.